PHYSICAL REVIEW E **94**, 062220 (2016)

Perturbation-free prediction of resonance-assisted tunneling in mixed regular-chaotic systems

Normann Mertig,[1,2,3] Julius Kullig,[1,2,4] Clemens Löbner,[1,2] Arnd Bäcker,[1,2] and Roland Ketzmerick[1,2]
[1]*Technische Universität Dresden, Institut für Theoretische Physik and Center for Dynamics, 01062 Dresden, Germany*
[2]*Max-Planck-Institut für Physik komplexer Systeme, Nöthnitzer Straße 38, 01187 Dresden, Germany*
[3]*Department of Physics, Tokyo Metropolitan University, Minami-Osawa, Hachioji 192-0397, Japan*
[4]*Institut für Theoretische Physik, Otto-von-Guericke-Universität Magdeburg, Postfach 4120, 39016 Magdeburg, Germany*
(Received 21 July 2016; published 28 December 2016)

For generic Hamiltonian systems we derive predictions for dynamical tunneling from regular to chaotic phase-space regions. In contrast to previous approaches, we account for the resonance-assisted enhancement of regular-to-chaotic tunneling in a nonperturbative way. This provides the foundation for future semiclassical complex-path evaluations of resonance-assisted regular-to-chaotic tunneling. Our approach is based on a new class of integrable approximations which mimic the regular phase-space region and its dominant nonlinear resonance chain in a mixed regular-chaotic system. We illustrate the method for the standard map.

DOI: 10.1103/PhysRevE.94.062220

I. INTRODUCTION

Tunneling is a fundamental effect in wave mechanics, which allows for entering classically inaccessible regions. While textbooks focus on tunneling through potential barriers, tunneling processes in nature often take place in the absence of such energetic barriers. Instead, one observes dynamical tunneling [1,2] between classically disjoint regions in phase space.

In generic Hamiltonian systems dynamical tunneling usually occurs between regions of regular and chaotic motion. For a typical phase space of a mixed regular-chaotic system, see Fig. 1(b). In particular, while a classical particle cannot traverse from the regular to the chaotic region, a wave can tunnel from the regular to the chaotic region. This regular-to-chaotic tunneling process manifests itself impressively in chaos-assisted tunneling [3,4].

Until today, the importance of regular-to-chaotic tunneling has been demonstrated in numerous experiments, including optical microcavities [5–10], microwave billiards [11–14], and cold-atom systems [15,16]. A recent success being the experimental verification [8,14] that tiny nonlinear resonance chains within the regular region, as shown in Fig. 1(b), indeed drastically enhance tunneling as predicted in Refs. [17–20]. Furthermore, regular-to-chaotic tunneling is expected to play an important role for atoms and molecules in strong fields, as discussed in Refs. [21–26].

Motivated by these applications regular-to-chaotic tunneling is also a field of intense theoretical research [12,25,27–42], which is mainly focused on periodically driven model systems with one degree of freedom. Here, a major achievement is the combination of (i) direct [33,38] and (ii) resonance-assisted [17–20] regular-to-chaotic tunneling in a single prediction [39,43]. This prediction shows that as a function of decreasing effective Planck's constant h one has two corresponding regimes: (i) Regular states localize on a single quantizing torus. In this regime, tunneling is determined by direct transitions from this regular torus into the chaotic region [33,38] which can be evaluated semiclassically using complex paths [40]. (ii) For even smaller h a regular state, while still mostly concentrated on the main quantizing torus, acquires resonance-assisted contributions on further quantizing tori [17–20] located more closely to the border of the regular region, see Fig. 2(c) of Sec. IV for an illustration. This resonance-assisted contribution dominates tunneling into the chaotic region [31,39,43]. Thus, one observes a resonance-assisted enhancement of regular-to-chaotic tunneling. For an example of this enhancement, see Fig. 1(a). Note that for much smaller h there is even a third regime for which regular states may localize within the resonance chain. This regime is not considered here.

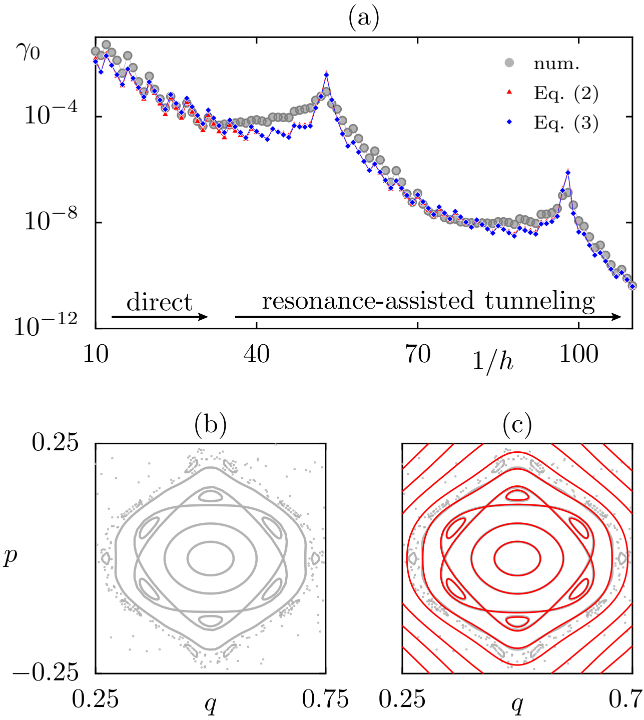

FIG. 1. (a) Regular-to-chaotic decay rate γ_0 versus $1/h$ for the standard map at $\kappa = 3.4$. The numerically determined rates (gray dots) are compared to (the sum of incoherent terms of) the predictions of Eq. (2) [(red) triangles] and Eq. (3) [(blue) squares]. (b) Phase space with regular orbits (lines) and a chaotic orbit (dots) including a 6:2 nonlinear resonance chain. (c) Like (b) with an integrable approximation [(red) lines] on top.

Despite the above achievements, a semiclassical evaluation of resonance-assisted tunneling in mixed regular-chaotic

2470-0045/2016/94(6)/062220(18)

systems remains an open problem. In particular, the state-of-the-art predictions [39,43] defy a semiclassical evaluation using the techniques developed for integrable systems [44,45]. More specifically, so far (i) an integrable approximation of the regular region which ignores resonance chains is used to predict the magnitude of direct tunneling transitions from quantizing tori towards the chaotic region [33,38]. Subsequently, (ii) resonance-assisted contributions are taken into account by perturbatively solving [20] an additional pendulum Hamiltonian which models the relevant resonance chain [39,43]. However, only a perturbation-free prediction, based on a single integrable approximation which includes the relevant resonance chain will allow for a semiclassical evaluation of resonance-assisted regular-to-chaotic tunneling in the spirit of Refs. [44,45].

In this paper we derive such perturbation-free predictions of resonance-assisted regular-to-chaotic tunneling. They are based on a new class of integrable approximations $H_{r:s}$ [46] which include the dominant $r{:}s$ resonance, see Fig. 1(c). In particular, the eigenvalue equation

$$\widehat{H}_{r:s}|m_{\text{int}}\rangle = E_m|m_{\text{int}}\rangle, \tag{1}$$

of such integrable approximations $H_{r:s}$ provides eigenstates $|m_{\text{int}}\rangle$ which model the localization of regular states on the regular phase-space region, explicitly including the resonance-assisted contributions on multiple quantizing tori, in a non-perturbative way. Using such states allows for extending the results of Refs. [33,38] to the case of resonance-assisted tunneling.

In particular, the decay rates γ_m of metastable states which localize on the regular phase-space region and decay via regular-to-chaotic tunneling can be predicted according to

$$\gamma_m \approx \Gamma_m(t=1) := \|\widehat{P}_{\mathcal{L}}\widehat{U}|m_{\text{int}}\rangle\|^2. \tag{2}$$

Here $\widehat{U}$ is the time evolution operator and $\widehat{P}_{\mathcal{L}}$ is a projector onto a leaky region $\mathcal{L}$ located in the chaotic part of the phase space.

We further show that regular-to-chaotic decay rates can be predicted with similar accuracy, when using a simplified formula which no longer contains the time-evolution operator. Instead, it evaluates only the probability of the state $|m_{\text{int}}\rangle$ on the leaky region $\mathcal{L}$,

$$\gamma_m \approx \Gamma_m(t=0) := \|\widehat{P}_{\mathcal{L}}|m_{\text{int}}\rangle\|^2. \tag{3}$$

Both perturbation-free predictions, Eqs. (2) and (3), give good results for the standard map, see Fig. 1, in that both predictions provide the foundation for future semiclassical predictions of resonance-assisted regular-to-chaotic tunneling [47]. We remark that the prediction of Eq. (2) has previously been evaluated semiclassically for integrable approximations without resonances [40], using the time-domain techniques of Refs. [27,28,34–36] giving predictions for direct regular-to-chaotic tunneling. However, we believe that a future semiclassical prediction of resonance-assisted regular-to-chaotic tunneling would be more easily obtained from Eq. (3), since it does not involve any time evolution and thus allows for a semiclassical evaluation using the simpler Wentzel-Kramer-Brillouin-(WKB)-like techniques of Refs. [44,45].

The paper is organized as follows: In Sec. II we introduce the standard map as a paradigmatic Hamiltonian example system with a mixed phase space. We further present regular-to-chaotic decay rates as a measure of regular-to-chaotic tunneling and discuss their numerical evaluation. In Sec. III we derive the predictions, Eqs. (2) and (3). In Sec. IV we illustrate how these predictions are evaluated using the example of the standard map. In Sec. V we present our results and compare them to the perturbative predictions of Refs. [39,43]. In Sec. VI we discuss the main approximations and limitations of our approach. A summary and outlook is given in Sec. VII.

II. EXAMPLE SYSTEM

In this paper we focus on periodically driven Hamiltonian systems with one degree of freedom, which exhibit all generic features of a mixed phase space. Classically, the stroboscopic map

$$U : (q_n, p_n) \mapsto (q_{n+1}, p_{n+1}), \tag{4}$$

describes the evolution of positions and momenta, (q,p), in phase space from time $t = n$ to $t = n + 1$ over one period of the external driving. Quantum-mechanically, the time evolution is given by the corresponding unitary time-evolution operator $\widehat{U}$.

In Sec. II A we introduce the standard map as a paradigmatic example of a periodically driven one-degree-of-freedom system with a mixed phase space. In Sec. II B we introduce regular-to-chaotic decay rates γ, as the central object of our investigation. Furthermore, we discuss their numerical computation. Particular attention is paid to nonlinear resonance chains and their quantum manifestations.

A. Standard map

Classically, the standard map originates from a periodically kicked Hamiltonian with one degree of freedom $H(q,p,t) = T(p) + V(q)\sum_{n\in\mathbb{N}}\delta(n-t)$. Here, $\delta(\cdot)$ is the Dirac δ function. For the standard map $T(p) = p^2/2$ and $V(q) = \kappa/(2\pi)^2\cos(2\pi q)$, where κ is the kicking strength. Its stroboscopic map U [48], Eq. (4), in its symmetrized version is given by

$$q_{n+1} = q_n + p_n + \frac{\kappa}{4\pi}\sin(2\pi q_n), \tag{5a}$$

$$p_{n+1} = p_n + \frac{\kappa}{4\pi}\sin(2\pi q_n) + \frac{\kappa}{4\pi}\sin(2\pi q_{n+1}), \tag{5b}$$

where (q_n, p_n) represents a phase-space point in the middle of the nth kick. For convenience, the standard map is considered on a torus $(q,p) \in [0,1[\times[-0.5,0.5[$ with periodic boundary conditions.

In this paper we mainly focus on kicking strength $\kappa = 3.4$. Here the phase space exhibits a large regular region which is centered around an elliptic fixed point, see Fig. 1(b). As expected from the theorems by Kolmogorov, Arnold, and Moser (KAM) [49–52], the regular region consists of one-dimensional invariant tori. Along these tori orbits of regular motion rotate around the fixed point. These tori are interspersed by nonlinear resonance chains, wherever s rotations of a regular orbit match r periods of the external driving [48,53,54].

For example, the standard map at $\kappa = 3.4$ has a dominant $r{:}s = 6{:}2$ resonance, leading to the six regular subregions in Fig. 1(b). Note that we choose the numbers r and s in the ratio $r{:}s$ such that r is the number of subregions of the resonance. The region of regular motion is embedded in a region of chaotic motion.

The quantum-mechanical analog of the stroboscopic map U is the unitary time-evolution operator [55–60]

$$\widehat{U} = \exp\left[-i\frac{V(\hat{q})}{2\hbar}\right]\exp\left[-i\frac{T(\hat{p})}{\hbar}\right]\exp\left[-i\frac{V(\hat{q})}{2\hbar}\right]. \tag{6}$$

Here $h = 2\pi\hbar$ is the effective Planck constant and $\hat{q}$ and $\hat{p}$ are the operators of position and momentum, respectively. Similarly to the classical case, we consider $\widehat{U}$ on a toric phase space, which leads to grids in position and momentum space [55–60],

$$\overline{q}_n = h(n+\theta_p), \quad \text{with} \quad \overline{q}_n \in [0,1], \tag{7a}$$

$$\overline{p}_n = h(n+\theta_q), \quad \text{with} \quad \overline{p}_n \in [-0.5,0.5], \tag{7b}$$

with $n \in \mathbb{N}$. This implies that the inverse of the effective Planck constant is a natural number $1/h = N \in \mathbb{N}$, giving the dimension of the Hilbert space. For the standard map, we choose the Bloch phase $\theta_p = 0$, while $\theta_q = 0$ if N is even and $\theta_q = 0.5$ if N is odd. This gives the finite-dimensional time-evolution operator in position representation,

$$\langle\overline{q}_n|\widehat{U}|\overline{q}_k\rangle = \frac{e^{-i\pi/4}}{\sqrt{N}}\exp\left\{i\,2\pi N\left[-\frac{V(\overline{q}_n)}{2} + \frac{(\overline{q}_n-\overline{q}_k)^2}{2} - \frac{V(\overline{q}_k)}{2}\right]\right\}, \tag{8}$$

with $n,k = 0,\dots,N-1$.

In the following, it is fundamental that eigenstates of a mixed regular-chaotic system can be classified according to their semiclassical localization on the regular or chaotic region, respectively. More specifically, chaotic states spread across the chaotic region [61–63], while regular states localize on a torus τ_m of the regular region which has quantizing action [64–66]

$$J_m := \frac{1}{2\pi}\oint_{\tau_m} p(q)\,dq = (m+1/2)\hbar, \tag{9}$$

labeled by an index $m \in \mathbb{N}$. In order to account for resonance-assisted tunneling, it is further indispensable to consider the finer structure of regular states. In particular, it will be crucial that a regular state m localizes not only on a dominant quantizing torus J_m. Instead, an $r{:}s$ resonance induces additional contributions on the tori J_{m+kr} with $k \in \mathbb{Z}$, see Refs. [17–20,67–69] and references therein.

B. Regular-to-chaotic decay rates in the standard map

In this section, we introduce regular-to-chaotic decay rates γ of an open system for quantifying regular-to-chaotic tunneling. Note that in closed systems chaos-assisted tunnel splittings [4] are an often-used alternative [38].

Our general approach for defining regular-to-chaotic decay rates proceeds in three steps: (a) We introduce a leaky region $\mathcal{L}$ within the chaotic part of phase space, (b) we determine the *decay rates* of its regular states, and (c) we classify the corresponding decay rates as *regular-to-chaotic decay rates*. Step (c) is justified because each regular state of the open system decays by regular-to-chaotic tunneling towards the chaotic region and subsequently enters the leaky region within the chaotic part of phase space.

More specifically, we proceed by (a) introducing a projector $\widehat{P}_{\mathcal{L}}$ which absorbs probability on a phase-space region $\mathcal{L}$ within the chaotic part of phase space. Based on this projector and the unitary time-evolution operator $\widehat{U}$ of the closed system, we define the time-evolution operator of the open system as

$$\widehat{U}_{\text{o}} = (\hat{\mathbf{1}} - \widehat{P}_{\mathcal{L}})\hat{U}(\hat{\mathbf{1}} - \widehat{P}_{\mathcal{L}}). \tag{10}$$

(b) We solve its eigenvalue equation,

$$\widehat{U}_{\text{o}}|m\rangle = \exp\left(i\phi_m - \frac{\gamma_m}{2}\right)|m\rangle. \tag{11}$$

Here, $|m\rangle$ represents a metastable, right eigenvector of the subunitary operator $\widehat{U}_{\text{o}}$. The corresponding eigenvalue is determined by an eigenphase ϕ_m and a decay rate γ_m. The latter describes the exponential decay of $|m\rangle$ in time. (c) We assign to each regular state $|m\rangle$ a label m according to its dominant localization on the quantizing torus J_m and refer to its decay rate γ_m as the regular-to-chaotic decay rate.

Specifically, for the standard map (a) we use

$$\mathcal{L} := \{(q,p)\mid q < q_l \quad \text{or} \quad q > q_r := 1 - q_l\} \tag{12}$$

and define the projector

$$\widehat{P}_{\mathcal{L}}|q\rangle = \chi(q)|q\rangle \quad \text{with} \quad \chi(q) = \begin{cases}1 & \text{for } (q,\cdot) \in \mathcal{L}\\ 0 & \text{for } (q,\cdot) \notin \mathcal{L}\end{cases}. \tag{13}$$

Here we choose q_l close to the regular-chaotic border. This ensures that γ_m, which depends on the choice of the leaky region $\mathcal{L}$, is dominated by tunneling from the regular towards the chaotic region. For a more detailed discussion, see Sec. VI A. (b) We compute the finite-dimensional matrix representation of $\widehat{U}_{\text{o}}$ for each value of $1/h \in \mathbb{N}$. To this end, we set all those entries in Eq. (8) equal to zero, for which either $\overline{q}_n$ or $\overline{q}_k$ are in the leaky region $\mathcal{L}$. We diagonalize the resulting $\widehat{U}_{\text{o}}$ numerically. (c) The regular-to-chaotic decay rates γ_m are labeled according to the dominant localization of $|m\rangle$ on the quantizing tori $J_m = \hbar(m+1/2)$.

We present the numerically obtained regular-to-chaotic decay rates γ_0 of the standard map at $\kappa = 3.4$ as a function of the inverse effective Planck constant [(gray) dots] in Fig. 1(a). The numerical results are consistent with the expectations from Refs. [39,43]: (i) For $1/h \lesssim 35$ the state $|0\rangle$ localizes on the torus J_0 such that the direct tunneling from J_0 to $\mathcal{L}$ dominates. In this regime, γ_0 decreases exponentially for decreasing h, which is a characteristic feature of direct transitions, see Ref. [33,38,40,70]. (ii) In the regime $1/h \gtrsim 35$ tunneling is enhanced by the 6:2 resonance. For $35 \lesssim 1/h \lesssim 80$ the resonance contribution of the state $|0\rangle$ on J_6 is significant such that the direct tunneling transition from J_6 to $\mathcal{L}$ dominates γ_m. This leads to a peak at $1/h = 53$, where the state $|0\rangle$ has half its weight on J_6. Finally, for $1/h \gtrsim 80$, the resonance contribution of $|0\rangle$ on J_{12} is significant such that direct tunneling from J_{12} to $\mathcal{L}$ dominates the decay rate γ_m, with a peak at $1/h = 98$. In Figs. 3(a) and 3(c) of Sec. V we show similar numerical rates [(gray) dots] for the standard map at $\kappa = 2.9$ and $\kappa = 3.5$ with dominating 10:3 and 6:2 resonances, respectively.

III. PERTURBATION-FREE PREDICTIONS OF RESONANCE-ASSISTED REGULAR-TO-CHAOTIC TUNNELING

In this section we derive the perturbation-free predictions for resonance-assisted regular-to-chaotic decay rates. In Sec. III A we derive Eq. (2), which uses the time-evolution operator. In Sec. III B we derive Eq. (3), which does not use the time-evolution operator.

A. Derivation of Eq. (2) with time evolution

The starting point for deriving Eq. (2) is the definition of the regular-to-chaotic decay rate γ_m from the appropriate eigenvalue problem. We use the same definitions as for the numerical determination of regular-to-chaotic decay rates, see Eqs. (10) and (11) of Sec. II B. They are repeated for convenience, namely a general subunitary operator,

$$\widehat{U}_{\mathrm{o}} := (\hat{\mathbf{1}} - \widehat{P}_{\mathcal{L}})\hat{U}(\hat{\mathbf{1}} - \widehat{P}_{\mathcal{L}}), \tag{14}$$

and its eigenvalue equation,

$$\widehat{U}_{\mathrm{o}}|m\rangle = \exp\left(i\phi_m - \frac{\gamma_m}{2}\right)|m\rangle. \tag{15}$$

Here, the unitary operator $\widehat{U}$ describes the time evolution of a mixed regular-chaotic system over one unit of time. Furthermore, $\widehat{P}_{\mathcal{L}}$ is a projection operator which absorbs probability on the leaky region $\mathcal{L}$ within the chaotic part of phase space.

For decay rates of such systems, it can be shown that the following formula applies, see Appendix A for details,

$$\gamma_m = -\log(1 - \|\widehat{P}_{\mathcal{L}}\widehat{U}|m\rangle\|^2) \overset{\gamma_m \ll 1}{\approx} \|\widehat{P}_{\mathcal{L}}\widehat{U}|m\rangle\|^2, \tag{16}$$

i.e., a regular-to-chaotic decay rate γ_m (for which $\gamma_m \ll 1$) is given by the probability transfer from the regular state $|m\rangle$ into the leaky region $\mathcal{L}$ via the unitary time-evolution operator $\widehat{U}$. Equation (16) is as such not useful, since it still contains the unknown eigenvector $|m\rangle$. In particular, it would require to solve Eq. (15), which defines γ_m in the first place. Hence, we proceed in the spirit of Refs. [33,38], i.e., we approximate $|m\rangle$ using the eigenstates $|m_{\mathrm{int}}\rangle$ of an integrable approximation $H_{r:s}$, leading to our prediction of Eq. (2).

The key point of this paper is the use of an integrable approximation $H_{r:s}$, which includes the dominant r:s resonance. This ensures that $|m_{\mathrm{int}}\rangle$ models not only the localization of $|m\rangle$ on the main quantizing torus J_m but also accounts for the resonance-assisted contributions on the tori J_{m+kr}. Precisely this extends Eq. (2), as previously used in Refs. [33,38] for direct tunneling, to the regime of resonance-assisted regular-to-chaotic tunneling in a nonperturbative way.

B. Derivation of Eq. (3) without time evolution

In this section we derive Eq. (3). It predicts regular-to-chaotic decay rates from the localization of the mode $|m_{\mathrm{int}}\rangle$ on the leaky region $\mathcal{L}$. In contrast to Eq. (2), it does not use the time-evolution operator, in that, Eq. (3) is an ideal starting point for future semiclassical predictions of regular-to-chaotic decay rates [47] in the spirit of Refs. [44,45]. In particular, it avoids the complications which arise in a semiclassical evaluation of Eq. (2) due to the time-evolution operator. We further remark that predictions like Eq. (3) are common for open systems. For regular-to-chaotic decay rates they have heuristically been used, e.g., in Refs. [20,29,30,43]. Here the main purpose of deriving Eq. (3) is to explicitly point out the involved approximations.

The derivation starts from an alternative definition of the subunitary time-evolution operator

$$\widehat{U}'_{\mathrm{o}} := \widehat{U}(\hat{\mathbf{1}} - \widehat{P}_{\mathcal{L}}), \tag{17}$$

which satisfies the eigenvalue equation

$$\widehat{U}'_{\mathrm{o}}|m'\rangle = \exp\left(i\phi_m - \frac{\gamma_m}{2}\right)|m'\rangle. \tag{18}$$

Compare with Eqs. (14) and (15). As shown in Appendix B, the operators $\widehat{U}_{\mathrm{o}}$ and $\widehat{U}'_{\mathrm{o}}$ are isospectral. Therefore, they exhibit the same eigenvalues, which give rise to the same regular-to-chaotic decay rates γ_m. Furthermore, the corresponding normalized right eigenvectors can be transformed into each other, see Appendix B. We find

$$|m\rangle = \frac{1}{\exp\left(i\phi_m - \frac{\gamma_m}{2}\right)}(\hat{\mathbf{1}} - \widehat{P}_{\mathcal{L}})|m'\rangle, \tag{19}$$

which implies that $|m\rangle$ and $|m'\rangle$ localize on the quantizing tori J_{m+kr} of the regular region with equal probability (for $\gamma_m \ll 1$). On the other hand, $|m'\rangle$ is the time-evolved mode $|m\rangle$ according to

$$|m'\rangle = \widehat{U}|m\rangle. \tag{20}$$

Inserting Eq. (20) into Eq. (16) gives

$$\gamma_m = -\log(1 - \|\widehat{P}_{\mathcal{L}}|m'\rangle\|^2) \overset{\gamma_m \ll 1}{\approx} \|\widehat{P}_{\mathcal{L}}|m'\rangle\|^2, \tag{21}$$

which shows that a regular-to-chaotic decay rate γ_m (for which $\gamma_m \ll 1$) is equivalent to the probability to find $|m'\rangle$ on the leaky region $\mathcal{L}$. Similarly to Eq. (16), Eq. (21) is as such not helpful, because it still contains the eigenvector $|m'\rangle$. In particular, it would require to solve Eq. (18), which defines γ_m in the first place. Hence, we approximate the mode $|m'\rangle$ using the more accessible eigenstates $|m_{\mathrm{int}}\rangle$ of an integrable approximation $H_{r:s}$, leading to our prediction of Eq. (3).

Here the key point is again the use of integrable approximations $H_{r:s}$ which includes the relevant r:s resonance. Therefore, $|m_{\mathrm{int}}\rangle$ models not only the localization of $|m'\rangle$ on the main quantizing torus J_m but also its resonance-assisted contributions on the tori J_{m+kr}. Precisely, this allows for predicting resonance enhanced regular-to-chaotic decay rates from Eq. (3) in a nonperturbative way.

An application of the predictions, Eqs. (2) and (3), for the standard map is demonstrated in Sec. IV. The key approximation, i.e., modeling metastable regular states $|m\rangle$ (or $|m'\rangle$) in terms of eigenstates $|m_{\mathrm{int}}\rangle$ of an integrable approximation $H_{r:s}$, is discussed in Sec. VI B. Moreover, a comparison of the nonperturbative predictions, Eqs. (2) and (3), to the perturbative predictions of Refs. [39,43] is given in Sec. V B.

IV. PERTURBATION-FREE PREDICTION OF TUNNELING IN THE STANDARD MAP

In this section we illustrate our approach by applying it to the standard map. In Sec. IV A, we determine the $r{:}s$ resonance which dominates tunneling. In Sec. IV B, we set up an integrable approximation including the nonlinear resonance chain using the iterative canonical transformation method [46,71] as presented in Ref. [46]. In Sec. IV C, we quantize the integrable approximation and determine its eigenstates $|m_{\text{int}}\rangle$ from Eq. (1). Finally, the results will be discussed in Sec. V.

A. Choosing the relevant resonance

In order to apply our prediction it is crucial to first identify the $r{:}s$ resonance which dominates the tunneling process. A detailed discussion as to which resonance dominates tunneling in which regime can be found in Ref. [39]. Here we focus on the $r{:}s$ resonance of lowest order r, which dominates the numerically and experimentally relevant regime where $\gamma > 10^{-15}$.

The area covered by the subregions of such a resonance can be very small; see the inset of Fig. 3(a). Therefore, it is necessary to search for resonances systematically. To this end, we determine the frequencies of orbits within the regular region, as described in Ref. [46]. We then identify the $r{:}s$ resonance of lowest order r by searching for the rational frequencies $2\pi s/r$ with smallest possible denominator.

Specifically, for the standard map, parity implies that r has to be an even number in order to reflect the correct number of subregions forming the resonance chain. For the examples we consider in this paper, we find a dominant 10:3 resonance for $\kappa = 2.9$ and a dominant 6:2 resonance for both $\kappa = 3.4$ and $\kappa = 3.5$.

B. Integrable approximation of a regular region including a resonance chain

In order to determine an integrable approximation of the regular region which includes the dominant $r{:}s$ resonance, we use the method introduced in Ref. [46]. Here we briefly summarize the key points.

The integrable approximation $H_{r:s}(q,p)$ of Ref. [46] is generated in two steps. First, the normal-form Hamiltonian is defined as

$$\mathcal{H}_{r:s}(\theta,I) = \mathcal{H}_0(I) + 2V_{r:s}\left(\frac{I}{I_{r:s}}\right)^{r/2}\cos(r\theta+\phi_0), \tag{22a}$$

$$\mathcal{H}_0(I) = \frac{(I-I_{r:s})^2}{2M_{r:s}} + \sum_{n=3}^{N_{\text{disp}}} h_n(I-I_{r:s})^n. \tag{22b}$$

It contains the essential information on the regular region in the corotating frame of the resonance. This Hamiltonian is precisely the effective pendulum Hamiltonian used in Ref. [39,43]. Here, $\mathcal{H}_0(I)$ is a polynomial of low order N_{disp}, chosen such that its derivative fits the actions and frequencies of the regular region in the corotating frame of the resonance. The action of the resonant torus is $I_{r:s}$. The parameters $M_{r:s}$ and $V_{r:s}$ are determined from the size of the resonance regions in the mixed system as well as the stability of its central orbit [31]. Finally, ϕ_0 is used to control the fixed-point locations of the resonance chain.

In a second step, a canonical transformation

$$\mathcal{T} : (\theta,I) \mapsto (q,p) \tag{23}$$

is used to adapt the tori of the effective pendulum Hamiltonian to the shape of the regular region in (q,p) space, giving the Hamilton function

$$H_{r:s}(q,p) = \mathcal{H}_{r:s}(\mathcal{T}^{-1}(q,p)). \tag{24}$$

The transformation $\mathcal{T}$ is composed of (i) a harmonic oscillator transformation to the fixed point of the regular region $\mathcal{T}^0$, Eq. (C1), which provides a rough integrable approximation and (ii) a series of canonical near-identity transformations $\mathcal{T}^1,\ldots,\mathcal{T}^{N_\mathcal{T}}$, Eq. (C2), which improve the agreement between the shape of tori of the mixed system and the integrable approximation.

Note that a successful prediction of decay rates requires an integrable approximation which provides a smooth extrapolation of tori into the chaotic region [33,38]; see insets of Fig. 3. This is ensured by using simple near-identity transformations $\mathcal{T}^1,\ldots,\mathcal{T}^{N_\mathcal{T}}$, i.e., low orders N_q,N_p in Eq. (C2). For further details the reader is referred to Ref. [46] and Appendix C, where it is described how the integrable Hamiltonians for the standard map at $\kappa = 2.9$, $\kappa = 3.4$, and $\kappa = 3.5$, see insets of Fig. 3, are generated.

C. Quantization of the integrable approximation

In the following, we summarize the quantization procedure for the integrable approximation. The details are discussed in Appendix C 2. In its final form, this quantization procedure is almost identical to the approach presented in Ref. [39]. It consists of two steps: (Q1) The integrable approximation without resonance is used to construct states which localize along a single quantizing torus of the regular region. (Q2) The mixing of states, localizing along a single quantizing torus, is described by solving the quantization of the effective pendulum Hamiltonian, Eq. (22), introduced in Ref. [43]. Combining (Q1) and (Q2) gives the sought-after eigenstate $|m_{\text{int}}\rangle$ of the integrable approximation which includes the resonance.

More specifically: (Q1) We use the canonical transformation, Eq. (23), in order to define the function $I(q,p)$. Its contours approximate the tori of the regular phase-space region, ignoring the resonance chain. It thus resembles the role of the integrable approximation, previously used in Refs. [33,38,39]. The Weyl quantization of this function on a phase-space torus gives a Hermitian matrix,

$$\begin{aligned}\langle \bar{q}_n|\hat{I}|\bar{q}_m\rangle &= \frac{1}{2N}\sum_{l=0}^{2N-1}\exp\left(\frac{i}{\hbar}(\bar{q}_n-\bar{q}_m)\,\bar{p}_{\frac{l}{2}}\right)\\ &\quad\times\left[I\left(\frac{\bar{q}_n+\bar{q}_m}{2},\bar{p}_{\frac{l}{2}}\right)+(-1)^l I\left(\frac{\bar{q}_n+\bar{q}_m+M_q}{2},\bar{p}_{\frac{l}{2}}\right)\right].\end{aligned} \tag{25}$$

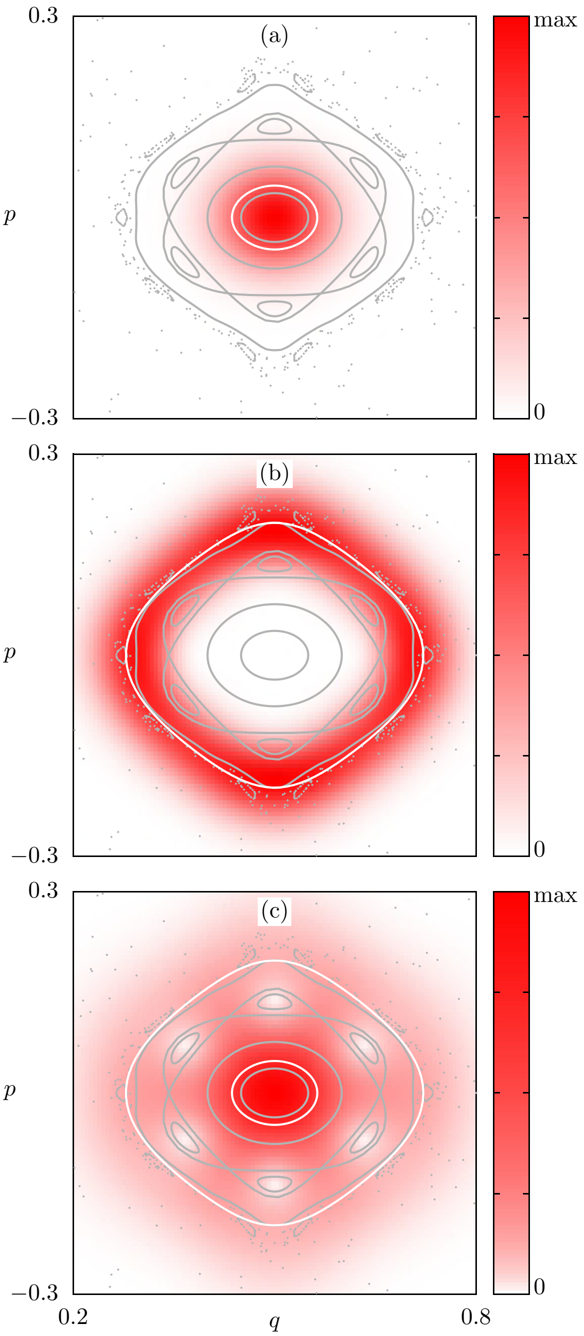

FIG. 2. [(a) and (b)] Husimi representation of $|I_n\rangle$ for the standard map at $\kappa = 3.4$ for (a) $n = 0$ and (b) $n = 6$ at $1/h = 53$. Regular tori (gray lines) and chaotic orbits (dots) illustrate the phase space. The quantizing tori of $H_{r:s}$ for $V_{r:s} = 0$ are shown by a thick (white) line. (c) Approximate mode $|m_{\text{int}}\rangle$ for $m = 0$.

Solving its eigenvalue equation gives states $\langle \overline{q}_l | I_n \rangle$ which localize along a single contour of $I(q,p)$ with quantizing action $I_n = \hbar(n + 1/2)$. These states model the localization of states along the tori of quantizing action J_n in the mixed system. For an illustration, see Figs. 2(a) and 2(b).

(Q2) In the second step, we model the mixing of states $\langle \overline{q}_l | I_n \rangle$ due to the nonlinear resonance chain. To this end, we follow Refs. [39,43] and consider the quantization of the effective pendulum Hamiltonian, Eq. (22), given by

$$\begin{aligned}
&\langle I_m | \widehat{\mathcal{H}}_{r:s} | I_n \rangle \\
&\quad = \mathcal{H}_0(I_n)\, \delta_{m,n} + V_{r:s} \left(\frac{\hbar}{I_{r:s}} \right)^{r/2} \\
&\qquad \times \left(e^{-i\phi_0} \sqrt{\frac{n!}{(n-r)!}}\, \delta_{m,n-r} + e^{i\phi_0} \sqrt{\frac{(n+r)!}{n!}}\, \delta_{m,n+r} \right).
\end{aligned} \tag{26}$$

Solving this eigenvalue problem gives the sought-after state in the basis of quantizing actions $\langle I_n | m_{\text{int}} \rangle$. Note that the matrix in Eq. (26) couples basis states $|I_n\rangle$ and $|I_{n'}\rangle$ only if $|n' - n| = kr$. Thus, the coefficients $\langle I_n | m_{\text{int}} \rangle$ are nonzero only if $n = m + kr$. This is called the selection rule of resonance-assisted tunneling. Combining (Q1) and (Q2) results in the mode expansion

$$\langle \overline{q}_l | m_{\text{int}} \rangle = \sum_k \langle \overline{q}_l | I_{m+kr} \rangle \langle I_{m+kr} | m_{\text{int}} \rangle. \tag{27}$$

For an illustration of a state $|m_{\text{int}}\rangle$, see Fig. 2(c). Note that its Husimi function exhibits exactly the morphology discussed in Ref. [68].

We now make a couple of remarks: (a) We use the above quantization procedure, rather than directly applying the Weyl rule to $H_{r:s}(q,p)$, Eq. (24), in order to explicitly enforce the selection rule of resonance-assisted tunneling. (b) The ad hoc two-step quantization scheme avoids the problem of defining the quantum counterpart for the canonical transformations $\mathcal{T}^1, \ldots, \mathcal{T}^{N_\mathcal{T}}$, Eq. (C2), used in the classical construction of the integrable approximation, see Sec. C 2 in the Appendix for details. (c) The above quantization is almost identical to the procedure used in Refs. [39,43]. This allows for a direct comparison to the results of Refs. [39,43], see Sec. V B. (d) The quantization procedure cannot determine the relative phase between the terms in the mode expansion of Eq. (27).

In order to understand the relative phase recall: (i) The coefficient vector $\langle I_{m+kr} | m_{\text{int}} \rangle$ is determined by solving the eigenvalue problem of Eq. (26). Hence, it is determined up to a global phase ξ_m. (ii) The coefficient vectors $\langle \overline{q}_l | I_{m+kr} \rangle$ are determined by solving the eigenvalue problem of Eq. (25). Hence, each coefficient vector is determined up to a global phase φ_{m+kr}. Therefore, (i) changing the phase of the coefficient vector $\langle I_{m+kr} | m_{\text{int}} \rangle$ in Eq. (27) changes the global phase of $\langle \overline{q}_l | m_{\text{int}} \rangle$. This has no consequences for predicting decay rates. However, (ii) changing the phases φ_{m+kr} of each coefficient vector $\langle \overline{q}_l | I_{m+kr} \rangle$ changes the relative phase of contributions in Eq. (27). This changes the interference between the contributions to the sum in Eq. (27) and affects the predicted decay rates.

So far the phase issue was avoided by neglecting interference terms in the tunneling predictions [39,43]. For the symmetrized standard map, we propose to define the phases as follows: (i) Equation (26) gives a real symmetric matrix. This allows for choosing real coefficients $\langle I_n | m_{\text{int}} \rangle$ such that $\langle I_m | m_{\text{int}} \rangle > 0$. (ii) Equation (25) also gives a real symmetric matrix. This allows for choosing real coefficients $\langle \overline{q}_l | I_n \rangle$. Choosing the sign of these coefficients is discussed in Sec. C 2 in the Appendix. The main idea is to exploit the eigenstates of the harmonic oscillator which approximates the central fixed point of the regular region. For these harmonic oscillator states the relative phase is well defined. Then we choose the sign of $\langle \overline{q}_l | I_n \rangle$ such that its overlap with the corresponding eigenstate of the harmonic oscillator is positive, Eq. (C29).

V. RESULTS

We now apply the above procedure to the standard map at $\kappa = 2.9$, 3.4, and 3.5. This gives eigenstates $|m_{\text{int}}\rangle$ which we insert into our predictions, Eqs. (2) and (3). The necessary time-evolution operator, used in Eq. (2), is given by Eq. (8). The projector is defined by Eq. (13) using $q_l = 0.27, 0.26, 0.25$, respectively. The results are shown in Fig. 3. The numerically determined rates and the predicted rates are overall in good qualitative agreement. In both cases, they deviate from the exact numerical rates by at most two orders of magnitude, in that the accuracy of the perturbation-free predictions, Eq. (2) and Eq. (3), is equivalent to perturbative predictions from Refs. [39,43]. This establishes Eqs. (2) and (3) as state-of-the-art perturbation-free predictions of resonance-assisted regular-to-chaotic tunneling. See Sec. V B for a detailed comparison.

A. Incoherent predictions and quantum phase

As discussed in Sec. IV C, our quantization scheme cannot determine the relative phases between the contributions of Eq. (27) for a system without time-reversal symmetry. In the following, we discuss the consequences of such an undetermined phase for the prediction of decay rates. To this end, we summarize our predictions, Eqs. (2) and (3), in the following compact form:

$$\Gamma_m(t) := \| \widehat{P}_{\mathcal{L}} \widehat{U}^t |m_{\text{int}}\rangle \|^2, \tag{28}$$

where $t = 1$ denotes the prediction based on time evolution and $t = 0$ denotes the prediction without time evolution. Now we insert the mode expansion, Eq. (27), and average over the undetermined phases φ_{m+kr} of the coefficient vectors $\langle \overline{q}_l | I_{m+kr} \rangle$. This gives the incoherent prediction

$$\Gamma_m^{\text{inc}}(t) := \sum_k \Gamma_{m,m+kr}^{\text{diag}}(t), \tag{29}$$

where the diagonal term $\Gamma_{m,n}^{\text{diag}}(t)$ is the contribution of the state $|I_n\rangle$ to the incoherent prediction as

$$\Gamma_{m,n}^{\text{diag}}(t) := |\langle I_n | m_{\text{int}} \rangle|^2 \Gamma_n^d(t) \tag{30}$$

and

$$\Gamma_n^d(t) := \| \widehat{P}_{\mathcal{L}} \widehat{U}^t | I_n \rangle \|^2 \tag{31}$$

is the rate of direct regular-to-chaotic tunneling as previously introduced in Refs. [33,38].

The results based on Eq. (29) are shown in Fig. 4. As expected, the incoherent predictions, Eq. (29), and the full predictions, Eq. (28), agree very well in the regime where a single diagonal contribution dominates, i.e., in the regime of direct tunneling as well as the peak region. However, in between these regions there are always two diagonal contributions of similar magnitude, which can interfere. It is in these regions that we expect deviations between the predictions of Eq. (28) and the incoherent predictions of Eq. (29).

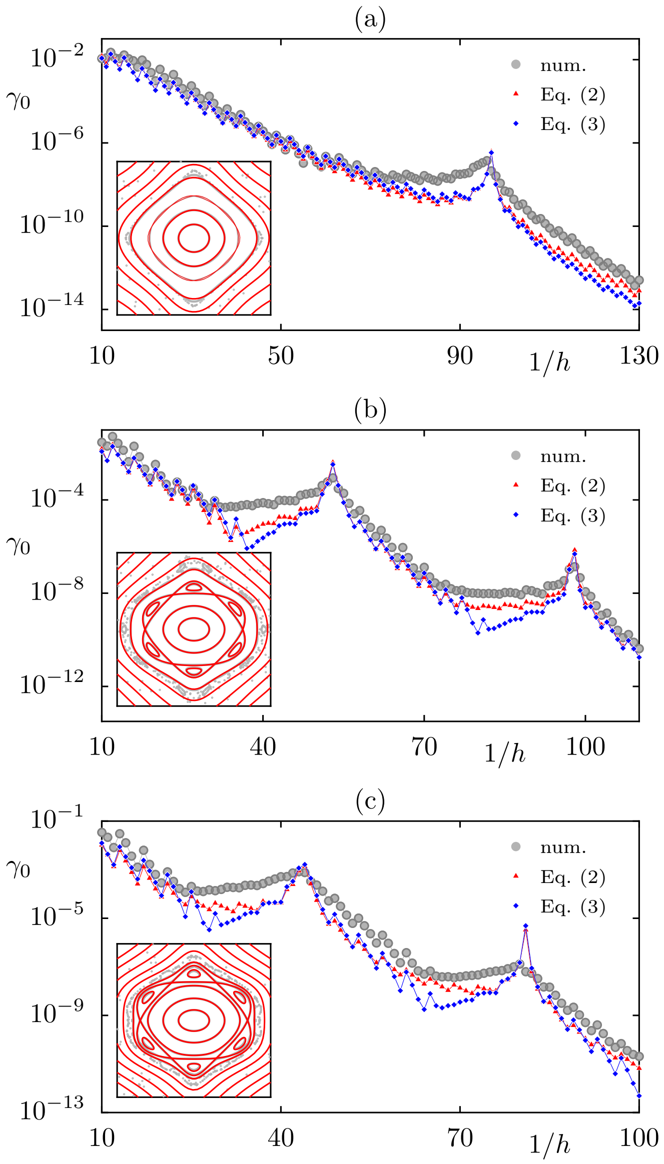

FIG. 3. Decay rates for the standard map at (a) $\kappa = 2.9$, (b) $\kappa = 3.4$, and (c) $\kappa = 3.5$ versus the inverse effective Planck constant $1/h$. Numerically determined rates (dots) are compared to predicted rates, using Eq. (2) [(red) triangles] and Eq. (3) [(blue) squares]. The insets show the corresponding phase space with regular tori [(gray) lines] and chaotic orbits (dots) with tori of the integrable approximation [(red) lines].

An example where this deviation is particularly large is the case of $\kappa = 3.4$ and $\kappa = 3.5$, see Figs. 4(b) and 4(c). Here Eq. (28) predicts destructive interference, which leads to a drastic suppression of the predicted decay rate. On the other hand, the phase-averaged, incoherent prediction, Eq. (29), does not predict such a drastic suppression. This leads to the counterintuitive situation that the incoherent prediction, Eq. (29), which was obtained from Eq. (28) by applying an additional approximation, describes the numerically determined decay rates better.

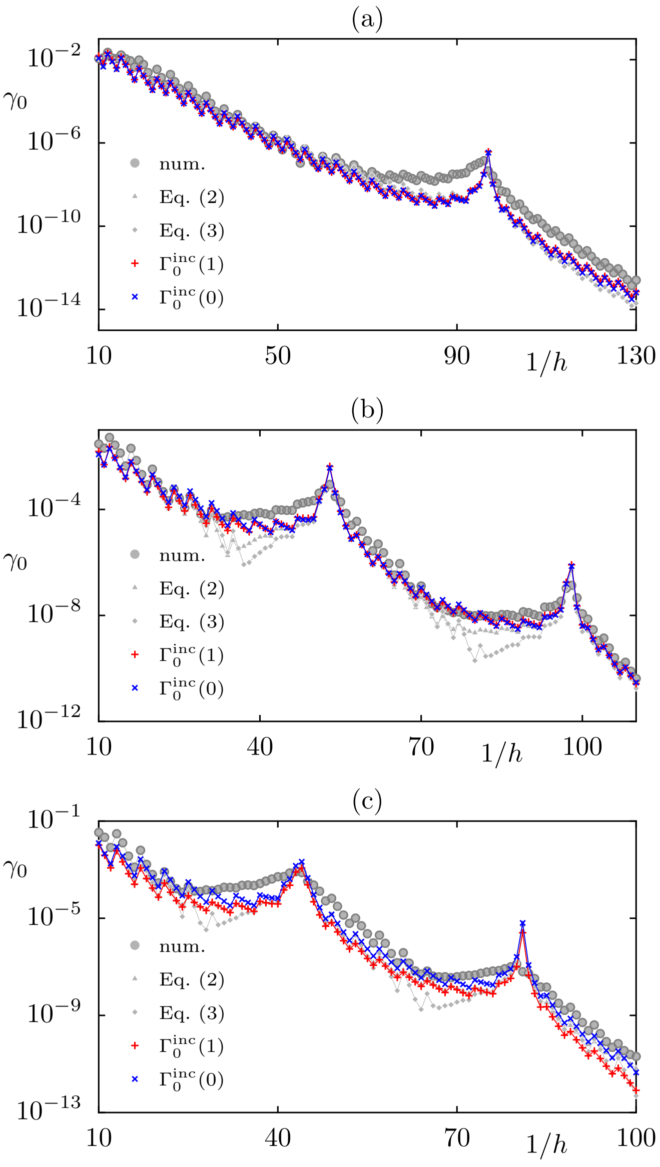

FIG. 4. Decay rates for the standard map at (a) $\kappa = 2.9$, (b) $\kappa = 3.4$, and $\kappa = 3.5$ versus the inverse effective Planck constant $1/h$. Numerically determined rates (dots) are compared to rates, predicted from incoherent terms according to Eq. (29), with $\Gamma_m^{\mathrm{inc}}(1)$ [(red) pluses] and $\Gamma_m^{\mathrm{inc}}(0)$ [(blue) crosses]. We further show predictions according to Eq. (2) [(gray) triangles] and Eq. (3) [(gray) squares].

This paradox can be explained as follows: A drastic suppression of decay rates can only be expected for exact destructive interference between the dominant contributions. On the other hand, any slight detuning of the dominant modes lifts the effect of destructive interference and restores the decay rate to the full magnitude of its contributions. In particular, it leads to a prediction much closer to the phase-averaged result, Eq. (29). Precisely this happens in our system, i.e., Eq. (28), based on $|m_{\mathrm{int}}\rangle$, predicts destructive interference. However, the contributions of the original eigenstate $|m\rangle$, approximated via $|m_{\mathrm{int}}\rangle$ in prediction (28), are slightly detuned from destructive interference, see Fig. 9(d) in Sec. VI C. This lifts the drastic suppression of decay rates and explains why the phase-averaged prediction, Eq. (29), is much closer to the exact, numerically determined rates.

These results highlight the relevance of the phase factor φ_{m+kr} for obtaining an accurate description of decay rates even between the resonance-assisted tunneling peaks. In previous studies of resonance-assisted tunneling in systems with a mixed phase space [39] this phase factor has been ignored by directly employing the incoherent predictions. Hence, a satisfactory theoretical treatment of the phase factor φ_{m+kr} so far does not exist. Clearly, our current approach is also insufficient. The precise reason is not clear to us. We expect that exploiting the symmetry of the integrable approximation in order to find a real representation of the approximate mode $\langle \overline{q}_l|m_{\mathrm{int}}\rangle$ is too naive, in particular, because it is used for approximating the metastable state $\langle \overline{q}_l|m\rangle$ of the open standard map, which can never admit an entirely real representation. For a detailed discussion of this point see Sec. VI C. Another possibility is that the phase factor in a nonintegrable system is beyond an integrable approximation.

B. Perturbative predictions

In this section, we compare our results to the perturbative predictions of Refs. [39,43]. This perturbative prediction is obtained by approximating the coefficient $\langle I_{m+kr}|m_{\mathrm{int}}\rangle$ in the incoherent prediction Eq. (29) by solving Eq. (26) perturbatively [43],

$$\langle I_{m+kr}|m_{\mathrm{int}}\rangle \approx \mathcal{A}^{(r:s)}_{m,m+kr} := \prod_{l=1}^{k} \frac{\langle I_{m+lr}|\widehat{\mathcal{H}}_{r:s}|I_{m+(l-1)r}\rangle}{\mathcal{H}_0(I_m) - \mathcal{H}_0(I_{m+kr})}. \quad (32)$$

Note that $\mathcal{H}_0(I)$ is considered in the corotating frame. This leads to

$$\Gamma_m^{\mathrm{per}}(t) := \sum_k \left|\mathcal{A}^{(r:s)}_{m,m+kr}\right|^2 \Gamma_m^d(t). \quad (33)$$

A slight difference of the above expression as compared to Ref. [39,43] is the use of the projector $\widehat{P}_{\mathcal{L}}$ rather than a projector on the whole chaotic region. Thus our prediction eliminates a free parameter from the perturbative predictions of Refs. [39,43]. The results of the perturbative predictions are presented in Fig. 5. They agree with the prediction obtained from Eq. (29), with the slight difference that the perturbative results deviate around the peak region.

We conclude this section with a short list of advantages and disadvantages of the perturbation-free and perturbative predictions as follows:

(i) The perturbation-free framework, Eqs. (2) and (3), as well as their incoherent version, Eq. (29), predict numerical rates with similar accuracy as the perturbative framework of Refs. [39,43].

(ii) One advantage of the perturbative prediction is the possibility to evaluate the terms $\langle I_m|m_{\mathrm{int}}\rangle$ analytically, Eq. (32). Yet, for practical use, even the perturbative approach requires an integrable approximation for predicting the direct rates Γ_m^d. Hence, both predictions are equally challenging in their implementation.

(iii) Another advantage of the perturbative prediction is the possibility to include multiple resonances into Eq. (33), which is not yet possible for the perturbation-free predictions presented in this paper. Note that this restriction is not

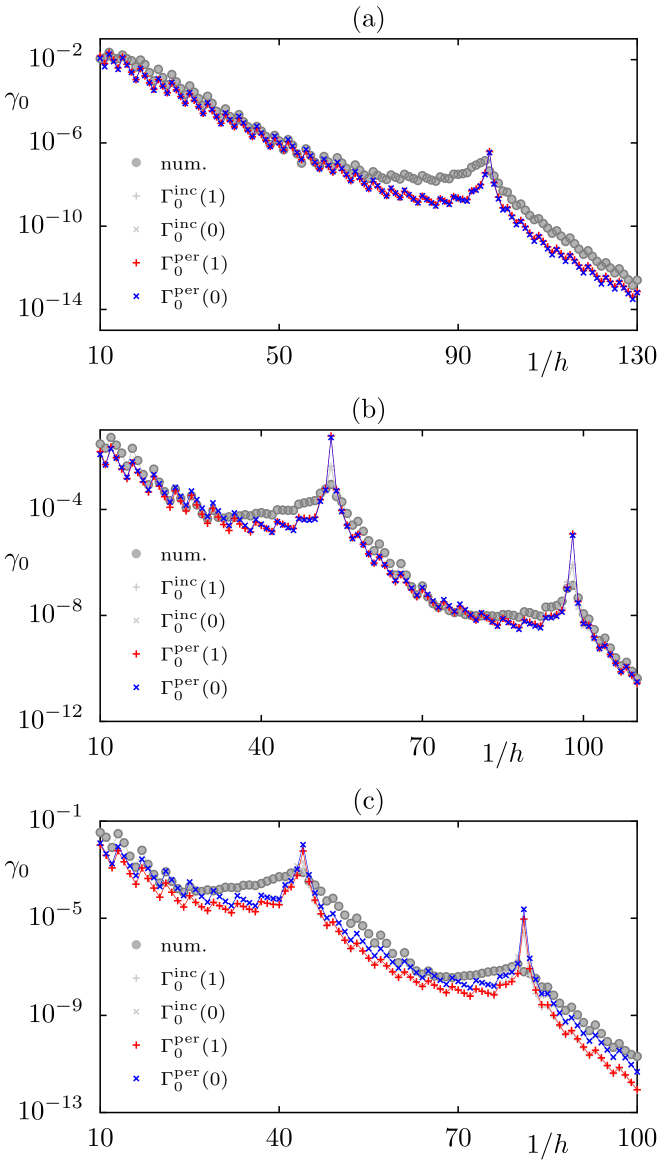

FIG. 5. Decay rates for the standard map at (a) $\kappa = 2.9$, (b) $\kappa = 3.4$, and (c) $\kappa = 3.5$ versus the inverse effective Planck constant $1/h$. Numerically determined rates (dots) are compared to rates, predicted perturbatively according to Eq. (33) with $\Gamma_m^{\mathrm{per}}(1)$ [(red) pluses] and $\Gamma_m^{\mathrm{per}}(0)$ [(blue) crosses]. We further show the prediction based on incoherent terms, according to Eq. (29) with $\Gamma_m^{\mathrm{inc}}(1)$ [(gray) pluses] and $\Gamma_m^{\mathrm{inc}}(0)$ [(gray) crosses].

too severe, because decay rates in the experimentally and numerically accessible regimes ($\gamma > 10^{-15}$) are typically affected by a single resonance only. Nevertheless, an extension of the perturbation-free results to the multiresonance regime is of theoretical interest and requires normal-form Hamiltonians $\mathcal{H}_{r:s}$ which include multiple resonances.

(iv) The main advantage of the perturbation-free framework is that it provides the foundation for deriving a future semiclassical prediction of resonance-assisted regular-to-chaotic tunneling [47].

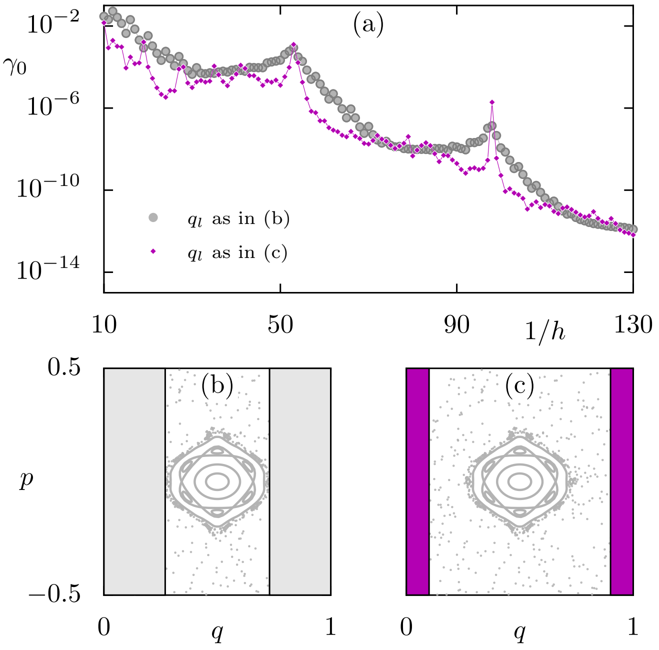

FIG. 6. Numerically determined decay rates γ_0 of the standard map at $\kappa = 3.4$ versus the inverse effective Planck constant $1/h$ for $q_l = 0.26$ [(gray) dots] and $q_l = 0.1$ [(magenta) squares]. [(b) and (c)] Phase space with shaded areas showing the leaky regions corresponding to q_l.

VI. DISCUSSION

In this section, we discuss several aspects of our results in detail. In Sec. VI A we discuss the dependence of decay rates on the choice of the leaky region. In Sec. VI B we compare the metastable states $|m\rangle$ and $|m'\rangle$ to the eigenstate $|m_{\mathrm{int}}\rangle$ of an integrable approximation. In Sec. VI C we analyze the approximation of $|m\rangle$ and $|m'\rangle$ via $|m_{\mathrm{int}}\rangle$ more systematically. In Sec. VI D we comment on the predictability of peaks.

A. Dependence of decay rates on the leaky region

This paper focuses entirely on situations where the leaky region $\mathcal{L}$ is chosen close to the regular-chaotic border region. However, in generic Hamiltonian systems like the standard map, the chaotic region is interspersed with partial barriers [72,73]. This leads to sticky motion in a hierarchical region surrounding the regular region. Furthermore, the chaotic component might be inhomogeneous and exhibit slow classical transport.

In view of these classical phenomena, it is not surprising that the numerical decay rates of the standard map, defined via Eqs. (15), depend on the choice of the leaky region via the parameter q_l. In order to illustrate this phenomenon, we show the numerically determined decay rate γ_0 of the standard map for two choices of the leaky region and two different κ parameters in Figs. 6 and 7, respectively.

In Fig. 6 we show results for the standard map at $\kappa = 3.4$. Here we compare (i) the regular-to-chaotic decay rates obtained for $q_l = 0.26$ [parameter used in this paper, (gray) dots] to (ii) decay rates obtained for $q_l = 0.1$ [(magenta) squares]. While the decay rates for $q_l = 0.26$ exhibit a rather

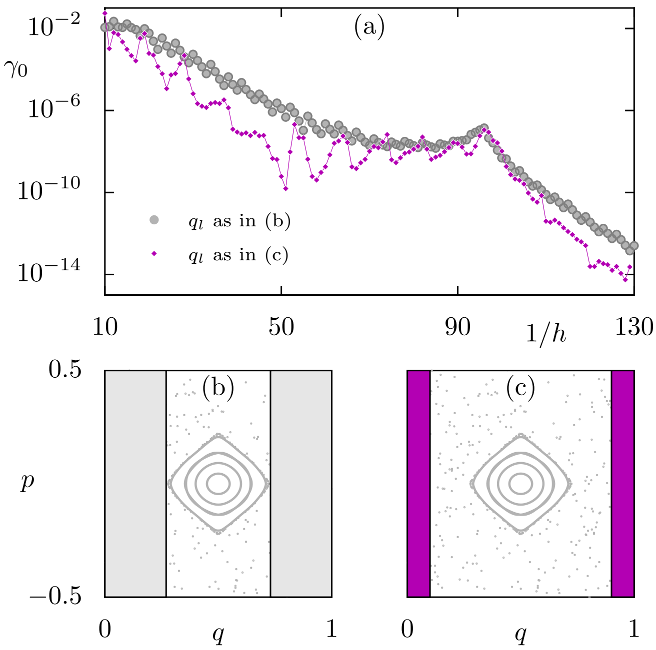

FIG. 7. Same as Fig. 6 for $\kappa = 2.9$ with $q_l = 0.27$ [(gray) dots] and $q_l = 0.1$ [(magenta) squares].

smooth behavior, the decay rates for $q_l = 0.1$ clearly exhibit additional oscillations and some overall suppression.

An even stronger deviation between regular-to-chaotic decay rates with varying leaky regions is observed in Fig. 7 for the standard map at $\kappa = 2.9$. Here (i) the decay rates as obtained for $q_l = 0.27$ [parameter used in this paper, (gray) dots] are compared to (ii) the decay rates obtained for $q_l = 0.1$ [(magenta) squares]. In addition to oscillations, the decay rates for $q_l = 0.1$ exhibit a clear suppression of their average value.

The origin of these deviations is unclear. The suppression of decay rates for leaky regions far from the regular-chaotic border could be due to slow transport through an inhomogeneous chaotic region from the regular-chaotic border towards the leaky region.

So far, a quantitative prediction of decay rates with leaky regions far from the regular-chaotic border remains an open problem. While varying the leaky region $\mathcal{L}$ close to the regular-chaotic border can be accounted for by our approach, predicting decay rates with leaky regions far from the regular-chaotic border is beyond our framework. In particular, while we observe that the numerical decay rates stabilize when pushing the leaky region away from the regular-chaotic border, the predicted rates continue to decrease exponentially.

So far, the best approach for dealing with this problem is to use an effective prediction [39,43]. To this end one argues that the numerical decay rate would not change much on pushing the boundary of the leaky region $\mathcal{L}$ beyond some effectively enlarged regular region $\mathcal{R}_{\text{eff}}$. See Ref. [43] for a discussion of $\mathcal{R}_{\text{eff}}$. Successively, one would approximate the projector onto the leaky region $\mathcal{L}$ in our predictions by the projector onto the complement of the effectively enlarged regular region $\mathcal{L}_{\text{eff}}$. This would result in an effective prediction Γ_m^{eff}.

Yet, there are several problems with such effective predictions: (a) Even though there are semiclassical arguments to define the effectively enlarged regular region in terms of partial barriers [43], replacing the leaky region $\mathcal{L}$ with some effective region $\mathcal{L}_{\text{eff}}$ introduces an effective parameter to the prediction. (b) Throughout this paper, we used leaky regions $\mathcal{L}$ which were almost tangential to the effectively enlarged regular regions discussed in Ref. [43]. Hence, replacing the region $\mathcal{L}$ with the effective region $\mathcal{L}_{\text{eff}}$ would not give results which are too far from the predictions discussed in this paper, i.e., even the effective predictions Γ_m^{eff} clearly deviates from numerically determined decay rates with leaky regions far from the regular region. (c) Even when using $\mathcal{L}_{\text{eff}}$ as a free fit parameter the effective prediction Γ_m^{eff} can at most capture the average behavior of numerical decay rates with a leaky region far from the regular-chaotic border. In particular, the oscillations observed for the numerical rates in Figs. 6 and 7 which span up to four orders of magnitude cannot be accounted for even by an effective theory.

Note that accurately predicting decay rates based on Eqs. (2) and (3), even for leaky regions far from the regular region, requires modes $|m_{\text{int}}\rangle$ which model the localization of $|m\rangle$ and $|m'\rangle$ even in the chaotic region. We expect that this is beyond the framework of an integrable approximation.

B. Metastable states and integrable eigenstates

We now discuss the key approximation of our predictions. To this end we compare the metastable states $|m\rangle$ and $|m'\rangle$ to the corresponding approximate state $|m_{\text{int}}\rangle$, which originates from an integrable approximation $H_{r:s}$ including the relevant resonance. We focus on a typical example using the states $m = m' = m_{\text{int}} = 0$ of the standard map at $\kappa = 3.4$ with $1/h = 55$ close to the first resonance peak in Fig. 1(a). The absolute squared values of the states in position representation are shown in Fig. 8. Here we compare (a) $|m\rangle$ to $|m_{\text{int}}\rangle$, (b) $|m'\rangle$ to $|m_{\text{int}}\rangle$, and (c) $|m'\rangle = \widehat{U}|m\rangle$ to $\widehat{U}|m_{\text{int}}\rangle$, depicting them with (gray) dots and (magenta) squares, respectively.

As a first conclusion, we see that the metastable states are well approximated by their integrable partners within the nonleaky region, i.e., the region between the dashed lines in Figs. 8(a)–8(c). In particular, both the metastable states and their integrable approximations exhibit the generic structure which is determined by the regular region and the dominant 6:2 resonance [19,20]: (i) A main Gaussian-like hump at $q = 0.5$ marks the main localization of the modes on the torus J_0. (ii) The decrease of the hump is interrupted at two side humps, which correspond to the resonance-assisted contribution of each mode on the torus J_6. From there, the Gaussian-like exponential decrease continues towards the leaky region, which is outside the dashed lines in Figs. 8(a)–8(c).

As a second conclusion from Fig. 8, we infer that beyond the regular-chaotic border, i.e., within the leaky region the metastable states deviate from their integrable counterparts. Here the integrable states continue to decrease exponentially. In contrast, the state $|m\rangle$ vanishes, see Fig. 8(a), while the state $|m'\rangle = \widehat{U}|m\rangle$, Eq. (20), decreases much slower, see Figs. 8(b) and 8(c).

Finally, we emphasize that $|m'\rangle$ and $|m_{\text{int}}\rangle$ agree for positions close to the regular-chaotic border. Furthermore, these contributions dominate the probability of $|m'\rangle$ and $|m_{\text{int}}\rangle$ on the leaky region. Precisely, this ensures that replacing

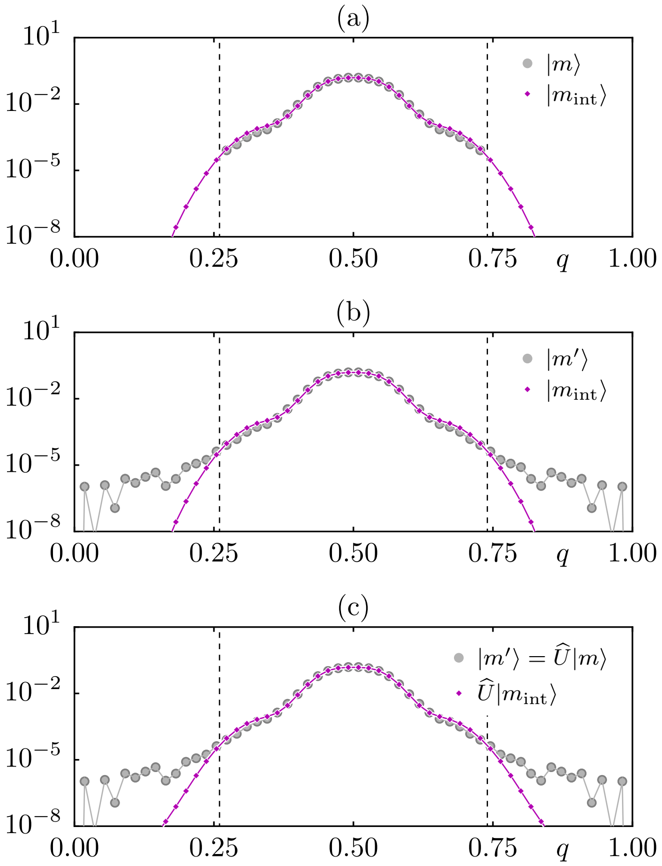

FIG. 8. For the standard map at $\kappa = 3.4$ with $1/h = 55$ we compare the position representation of (a) $|\langle q|m\rangle|^2$ to $|\langle q|m_{\text{int}}\rangle|^2$, (b) $|\langle q|m'\rangle|^2$ to $|\langle q|m_{\text{int}}\rangle|^2$, and (c) $|\langle q|\widehat{U}|m\rangle|^2$ to $|\langle q|\widehat{U}|m_{\text{int}}\rangle|^2$, depicting them with (gray) dots and (magenta) squares, respectively, for $m = m' = m_{\text{int}} = 0$. The dashed lines mark the positions q_l and $1 - q_l$ of the leaky region, as given in the text.

$|m'\rangle$ in the exact prediction, Eq. (21), by $|m_{\text{int}}\rangle$ results in a meaningful prediction according to Eq. (3). An analogous argument explains why replacing $\widehat{U}|m\rangle$ in the exact result, Eq. (16), by $\widehat{U}|m_{\text{int}}\rangle$ gives meaningful predictions according to Eq. (2).

C. Error analysis

In this section, we investigate the approximation of the metastable states $|m\rangle$ in the exact result Eq. (16) via the mode $|m_{\text{int}}\rangle$ in Eq. (2) from the perspective of Eq. (27), i.e., (i) we investigate the basis states $|I_n\rangle$ and (ii) the expansion coefficients $\langle I_n|m_{\text{int}}\rangle$. We focus on the standard map at $\kappa = 3.4$.

(i) In order to investigate our basis set $|I_n\rangle$, we expand the metastable state $|m\rangle$ in this basis and insert this expansion into the exact result (16). This gives

$$\gamma_m = \sum_n |\langle I_n|m\rangle|^2 \|\widehat{P}_{\mathcal{L}}\widehat{U}|I_n\rangle\|^2 + \sum_{n,n'} \langle m|I_{n'}\rangle\langle I_{n'}|\widehat{U}^\dagger \widehat{P}_{\mathcal{L}}^2 \widehat{U}|I_n\rangle\langle I_n|m\rangle. \tag{34}$$

Since the diagonal terms

$$\gamma_{m,n}^{\text{diag}} := |\langle I_n|m\rangle|^2 \|\widehat{P}_{\mathcal{L}}\widehat{U}|I_n\rangle\|^2 = |\langle I_n|m\rangle|^2 \Gamma_n^d(1) \tag{35}$$

provide a bound to the off-diagonal terms according to Cauchy's inequality,

$$|\langle m|I_{n'}\rangle\langle I_{n'}|\widehat{U}^\dagger \widehat{P}_{\mathcal{L}}^2 \widehat{U}|I_n\rangle\langle I_n|m\rangle| \leqslant \sqrt{\gamma_{m,n}^{\text{diag}}\gamma_{m,n'}^{\text{diag}}}, \tag{36}$$

we can interpret them as a way to quantify the contribution of the nth basis state $|I_n\rangle$ to the decay rate γ_m, in that $\gamma_{m,n}^{\text{diag}}$ takes a similar role as the contribution spectrum, discussed in Ref. [41].

In Fig. 9(a), we consider all contributions $\gamma_{0,n}^{\text{diag}}$ (lines) in comparison with the decay rate γ_0 (dots) for the standard map at $\kappa = 3.4$. While most contributions are two to three orders of magnitude smaller than γ_0, we find that the contributions $\gamma_{0,0}^{\text{diag}}$, $\gamma_{0,6}^{\text{diag}}$, and $\gamma_{0,12}^{\text{diag}}$ dominate. In order to further test whether the modes $|I_n\rangle$ with $n = 0,6,12$ are sufficient for describing γ_0, we sum the contributions $n,n' \in \{0,6,12\}$ of the dominant terms in Eq. (34). This gives the red triangles of Fig. 9(b). From these numerical observations we conclude that a reasonable description of γ_0 can be extracted using an approximate mode exclusively composed of states $|I_n\rangle$ with $n = 0,6,12,\ldots,$ as used in Eq. (27). However, it should be noted that the difference between γ_0 and its reduced version, based on contributions $n,n' \in \{0,6,12\}$ in Eq. (34), is already of the order of γ_0 itself. See the region $70 < 1/h < 100$ of Fig. 9(b) in particular. Hence, reducing the metastable state $|m\rangle$ to an approximate mode $|m_{\text{int}}\rangle$ using only basis states $|I_{m+kr}\rangle$ as in Eq. (27) can at best provide a reasonable backbone for describing the structure of γ_0. On the other hand, for our example a prediction of γ_0 where the remainder is smaller than the decay rate based on a reduced set of basis states $|I_n\rangle$ is only possible when summing over many additional contributions, even including $n \neq m + kr$. The precise origin of such contributions $\gamma_{m,n}^{\text{diag}}$ with $n \neq m + kr$ is currently under debate [41]: From the framework of resonance-assisted tunneling [19,20,39,43], we expect that the overlap $\langle I_n|m\rangle$ vanishes for $n \neq m + kr$. Hence, one might argue that the contributions $\gamma_{m,n}^{\text{diag}}$ with $n \neq m + kr$ arise in our example only because our basis $|I_n\rangle$ is insufficiently accurate to decompose $|m\rangle$ according to the theoretical expectation of resonance-assisted tunneling. On the other hand, the authors of Ref. [41] observe nonvanishing contributions $\langle I_n|m\rangle$ also for $n \neq m + kr$ even for a near-integrable situation, where an excellent integrable approximation exists. They argue that nonvanishing $\langle I_n|m\rangle$ should always occur and claim their treatment is beyond the current framework of resonance-assisted tunneling. Independent of the origin of the nonzero contributions $\gamma_{m,n}^{\text{diag}}$ for $n \neq m + kr$, their theoretical description is beyond the scope of this paper. In our examples the irrelevance of these contributions is ensured by choosing leaky regions close to the regular-chaotic border. However, for leaky regions far from the regular-chaotic border the contributions $\gamma_{m,n}^{\text{diag}}$ with $n \neq m + kr$ become relevant.

(ii) In the next step we evaluate the errors introduced by replacing the expansion coefficients $\langle I_{m+kr}|m\rangle$ by $\langle I_{m+kr}|m_{\text{int}}\rangle$ in Eq. (34). We focus on the corresponding diagonal contributions $\gamma_{m,m+kr}^{\text{diag}}$ and $\Gamma_{m,m+kr}^{\text{diag}}$, which represent the squared norm of the expansion coefficients $\langle I_{m+kr}|m\rangle$ and $\langle I_{m+kr}|m_{\text{int}}\rangle$ up

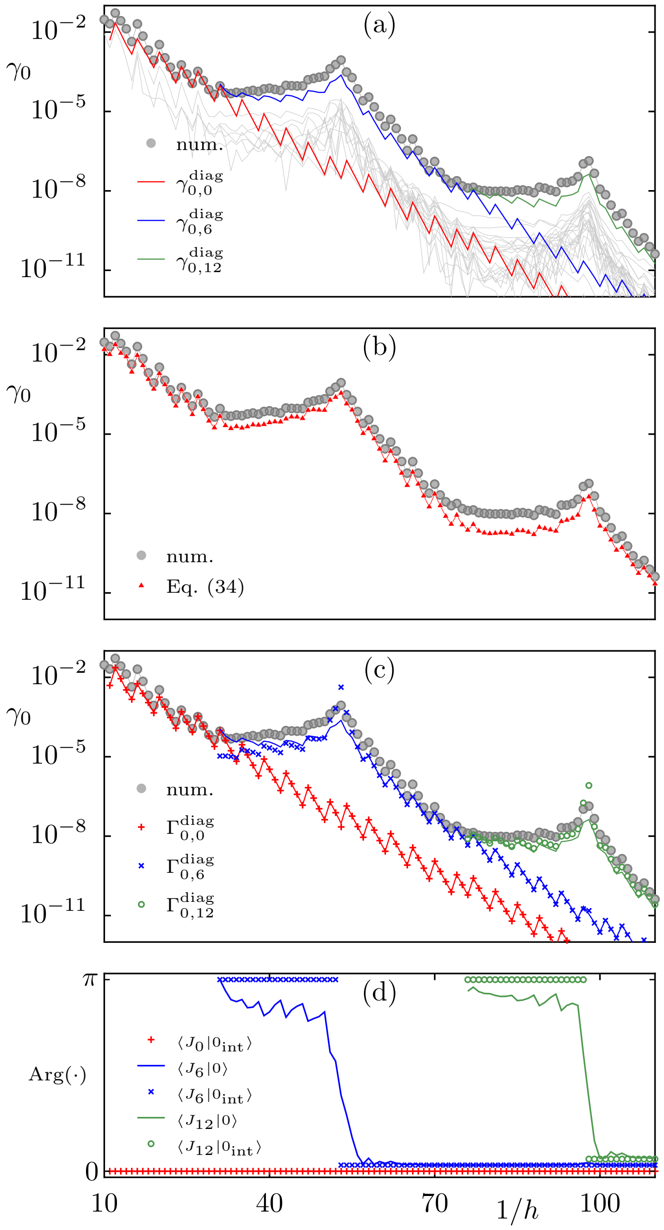

FIG. 9. Error analysis for the standard map at $\kappa = 3.4$. [(a)–(c)] The numerically determined rates [(gray) dots] and (d) the numerically determined phases Arg($\langle I_n|0\rangle$) for $n = 0,1,2$ (lines) are shown versus the inverse effective Planck constant $1/h$. (a) The contributions $\gamma_{0,n}^{\text{diag}}$, Eq. (35), are shown by lines. (b) The reduced prediction, Eq. (34) with $n,n' \in \{0,6,12\}$ is shown by (red) triangles. (c) The contributions $\gamma_{0,n}^{\text{diag}}$ of Eq. (35) (lines) are compared to $\Gamma_{0,n}^{\text{diag}}(1)$ of Eq. (30) (markers) for $n = 0,6,12$. (d) The phases Arg($\langle I_n|0\rangle$) (lines) and Arg($\langle I_n|0_{\text{int}}\rangle$) (markers) are compared for $n = 0,6,12$. (Phases close to zero are slightly shifted for $n = 6,12$ for visibility.)

to a multiplication by the direct rate $\Gamma_{m+kr}^{d}(1)$. See the lines and symbols in Fig. 9(c), respectively. From these data we conclude that the norm of $\langle I_{m+kr}|m_{\text{int}}\rangle$ provides a reasonable approximations for the norm of the expansion coefficients $\langle I_{m+kr}|m\rangle$. The deviations before each peak could be due to neglecting the higher-order action dependencies discussed in Ref. [43] in the Hamilton function of Eq. (22). Furthermore, we expect that the slightly broader peaks in the numerical rates $\gamma_{0,kr}^{\text{diag}}$ as compared to the sharper peaks of $\Gamma_{0,kr}^{\text{diag}}(1)$ observed for the integrable approximation are related to the openness of the mixed system.

Finally, in Fig. 9(d) we compare the phases Arg($\langle I_{m+kr}|m\rangle$) and Arg($\langle I_{m+kr}|m_{\text{int}}\rangle$) for $m = 0$ and $k = 0,1,2$, respectively. Here Arg$(\cdot) \in (-\pi,\pi]$ is the principal value of the complex argument function. Note that the global phase of $|m\rangle$ is fixed by setting Arg($\langle I_m|m\rangle$) $= 0$. The phases Arg($\langle I_{m+kr}|m_{\text{int}}\rangle$) are fixed as described in Sec. C 2 in the Appendix. While the phases of Arg($\langle I_{m+kr}|m_{\text{int}}\rangle$) jump from π to zero on traversing the peak for decreasing $1/h$ (change from destructive to constructive interference), their counterparts for Arg($\langle I_{m+kr}|m\rangle$) seem to follow this jump in a smoothed-out way. Compare symbols and lines in Fig. 9(d).

We attribute this phase detuning to the openness of the system, i.e., (a) the symmetries of the integrable approximation allow for choosing a real representation of the coefficient $\langle I_{m+kr}|m_{\text{int}}\rangle$. Its phase can thus only take values Arg($\langle I_{m+kr}|m_{\text{int}}\rangle$) $\in \{0,\pi\}$. In contrast, (b) the mode $|m\rangle$ originates from an open system and thus the coefficient $\langle I_{m+kr}|m\rangle$ is usually complex such that Arg($\langle I_{m+kr}|m\rangle$) might take any value.

While the deviation between the numerically determined phases Arg($\langle I_{m+kr}|m\rangle$) and the theoretically predicted phases Arg($\langle I_{m+kr}|m_{\text{int}}\rangle$) are seemingly small in Fig. 9(d), their deviation has huge effects on the predicted decay rate, i.e., (a) Eq. (2) predicts destructive interference of the diagonal terms in the region before each peak. This leads to strong deviations from the numerical decay rate, see Fig. 3(b). On the other hand, (b) already the minimal detuning of Arg($\langle I_{m+kr}|m\rangle$) from our prediction Arg($\langle I_{m+kr}|m_{\text{int}}\rangle$) is sufficient to lift the destructive interference. We assume that this explains why the incoherent prediction, Eq. (29), as illustrated in Fig. 4, describes the numerical rates much better than predictions according to, Eq. (2), see Fig. 4.

D. Predictability of peak positions

Finally, we discuss the predictability of peak positions. To this end we recall that $\mathcal{H}_0(I)$ in Eq. (22b) is determined by fitting its derivative to the numerically determined actions and frequencies $(\bar{\omega},\bar{J})$ of the regular phase-space region in the corotating frame. For an illustration, see Fig. 10. In particular, the data of the mixed system have a maximal action $\bar{J}_{\max}$, see the (black) dashed line in Fig. 10. Hence, $\mathcal{H}_0$ can be well controlled in the regular region $I < \bar{J}_{\max}$. However, for $I > \bar{J}_{\max}$, the function $\mathcal{H}_0$ is only an extrapolation to the chaotic region. Furthermore, the integrable approximation predicts a peak for γ_m [19,20,39,43] if

$$\mathcal{H}_0(I_m) = \mathcal{H}_0(I_{m+kr}), \tag{37}$$

where $I_m = \hbar(m + 1/2)$ and $I_{m+kr} = \hbar(m + kr + 1/2)$. This resonance conditions follows from Eq. (32).

However, for all examples presented in this paper the resonant torus I_{m+kr} is always located outside of the regular region, where $\mathcal{H}_0(I)$ is only given by an extrapolation. See Fig. 2(c) for an example of this situation. The (black) dots in Fig. 10(b) show the corresponding situation for $\mathcal{H}_0(I)$. In such a situation our approach cannot guarantee an accurate

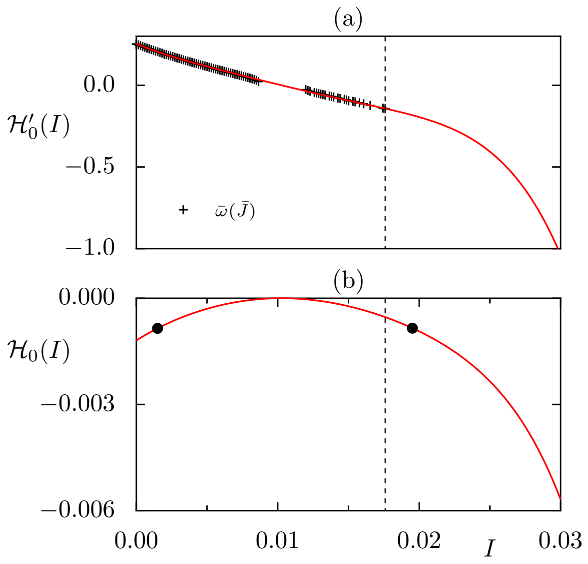

FIG. 10. For the standard map at $\kappa = 3.4$ we show (a) the fit of $\mathcal{H}_0'(I)$ (line) to the actions and frequencies of the regular region $(\bar{J},\bar{\omega})$ (crosses). (b) The function $\mathcal{H}_0(I)$ is shown as a (red) line. The two (black) dots show $(I_m,\mathcal{H}_0(I_m))$ and $(I_{m+kr},\mathcal{H}_0(I_{m+kr}))$ at $1/h = 53$. [(a) and (b)] The dashed line shows the position of $\bar{J}_{\max}$.

prediction of the peak position. Usually, this problem is not too severe and the extrapolation is good enough. An example where this problem appears can be seen in the second peak of Fig. 3(a) where the peak of the numerical decay rates and the predicted rates is shifted by $1/h = 1$.

VII. SUMMARY AND OUTLOOK

In this paper we present two perturbation-free predictions of resonance-assisted regular-to-chaotic decay rates, Eqs. (2) and (3). Both predictions are based on eigenstates $|m_{\text{int}}\rangle$ of an integrable approximation $H_{r:s}$, Eq. (1). The key point is the use of an integrable approximation $H_{r:s}$ of the mixed regular-chaotic system which includes the relevant nonlinear resonance chain. Therefore $|m_{\text{int}}\rangle$ models the localization of regular modes on the regular region, including resonance-assisted contributions in a nonperturbative way. This allows for extending the validity of Eq. (2), previously used for direct tunneling in Refs. [33,38], to the regime of resonance-assisted tunneling. Furthermore, we introduce a second prediction, Eq. (3), which no longer requires the time-evolution operator. Instead, it allows for predicting decay rates using the localization of the approximate mode on the leaky region, in that Eq. (3) provides an excellent foundation for a future semiclassical prediction of resonance-assisted regular-to-chaotic decay rates [47] in the spirit of Refs. [44,45]. The validity of the presented approach is verified for the standard map, where predicted and numerically determined regular-to-chaotic decay rates show good agreement.

Finally, we list future challenges: (a) The presented approach is so far limited to periodically driven systems with one degree of freedom. An extension to autonomous or periodically driven systems with two or more degrees of freedom is an interesting open problem. (b) The perturbation-free approach applies to the experimentally and numerically relevant regime, where a single resonance dominates regular-to-chaotic tunneling. Its extension to the semiclassical regime where multiple resonances affect tunneling is of theoretical interest. (c) The suppression of decay rates due to partial barriers is so far treated by choosing leaky regions close to the regular-chaotic region. Explicitly predicting the additional suppression of decay rates due to slow chaotic transport through inhomogeneous chaotic regions remains an open question.

ACKNOWLEDGMENTS

We gratefully acknowledge fruitful discussions with Jérémy Le Deunff, Felix Fritzsch, Yasutaka Hanada, Hiromitsu Harada, Kensuke Ikeda, Martin Körber, Steffen Löck, Amaury Mouchet, Peter Schlagheck, and Akira Shudo. We acknowledge support by the Deutsche Forschungsgemeinschaft (DFG) Grant No. BA 1973/4-1. N.M. acknowledges successive support by JSPS (Japan) Grant No. PE 14701 and Deutsche Forschungsgemeinschaft (DFG) Grant No. ME 4587/1-1.

APPENDIX A: DERIVATION OF EQ. (16)

In this Appendix we derive Eq. (16) starting from Eqs. (14) and (15). Taking the norm of the eigenvalue equation (15) for a normalized state $|m\rangle$ one finds

$$\begin{aligned}\exp(-\gamma_m) &= \|\widehat{U}_{\text{o}}|m\rangle\|^2 = \langle m|\widehat{U}_{\text{o}}^\dagger\widehat{U}_{\text{o}}|m\rangle\\ &= \langle m|(\hat{\mathbf{1}}-\widehat{P}_{\mathcal{L}})^\dagger\widehat{U}^\dagger(\hat{\mathbf{1}}-\widehat{P}_{\mathcal{L}})^\dagger(\hat{\mathbf{1}}-\widehat{P}_{\mathcal{L}})\widehat{U}(\hat{\mathbf{1}}-\widehat{P}_{\mathcal{L}})|m\rangle,\end{aligned} \tag{A1}$$

where in the last step the definition of $\widehat{U}_{\text{o}}$, Eq. (14), is used. We simplify this expression using

$$(\hat{\mathbf{1}}-\widehat{P}_{\mathcal{L}})|m\rangle = |m\rangle, \tag{A2}$$

which follows from Eqs. (14) and (15), giving

$$\exp(-\gamma_m) = \langle m|\widehat{U}^\dagger(\hat{\mathbf{1}}-\widehat{P}_{\mathcal{L}})^\dagger(\hat{\mathbf{1}}-\widehat{P}_{\mathcal{L}})\widehat{U}|m\rangle. \tag{A3}$$

Finally, exploiting the idempotence and hermiticity of the projector $\widehat{P}_{\mathcal{L}}$ gives

$$\begin{aligned}\exp(-\gamma_m) &= \langle m|\widehat{U}^\dagger\widehat{U}|m\rangle - \langle m|\widehat{U}^\dagger\widehat{P}_{\mathcal{L}}\widehat{U}|m\rangle\\ &= 1 - \|\widehat{P}_{\mathcal{L}}\widehat{U}|m\rangle\|^2,\end{aligned} \tag{A4}$$

where in the last step the unitarity of $\widehat{U}$ is used. From this follows the expression for regular-to-chaotic tunneling rates, Eq. (16).

APPENDIX B: ISOSPECTRALITY

In this Appendix, we demonstrate the isospectrality of the subunitary operators $\widehat{U}_{\text{o}}$ and $\widehat{U}_{\text{o}}'$ as defined by Eqs. (14) and (17), respectively. Furthermore, we discuss the transformation relating their eigenmodes. For convenience, we repeat the corresponding eigenvalue equations (15) and (18),

$$\widehat{U}_{\text{o}}|m\rangle = \lambda_m|m\rangle, \tag{B1}$$

$$\widehat{U}_{\text{o}}'|m'\rangle = \lambda_m'|m'\rangle, \tag{B2}$$

where the eigenvalues have been denoted by λ_m and λ'_m.

We now demonstrate the isospectrality of $\widehat{U}_{\rm o}$ and $\widehat{U}'_{\rm o}$. To this end we show:

(a) For each eigenstate $|m\rangle$ of $\widehat{U}_{\rm o}$ with eigenvalue λ_m, $\widehat{U}|m\rangle$ is an eigenstate of $\widehat{U}'_{\rm o}$ with the same eigenvalue λ_m,

$$\widehat{U}'_{\rm o}\widehat{U}|m\rangle \overset{(17)}{=} \widehat{U}(\widehat{\mathbf{1}} - \widehat{P}_{\mathcal{L}})\widehat{U}|m\rangle, \tag{B3}$$

$$\overset{(A2)}{=} \widehat{U}(\widehat{\mathbf{1}} - \widehat{P}_{\mathcal{L}})\widehat{U}(\widehat{\mathbf{1}} - \widehat{P}_{\mathcal{L}})|m\rangle, \tag{B4}$$

$$\overset{(14)}{=} \widehat{U}\widehat{U}_{\rm o}|m\rangle, \tag{B5}$$

$$\overset{(B1)}{=} \lambda_m\widehat{U}|m\rangle. \tag{B6}$$

This further shows that the normalized eigenmode $|m\rangle$ of $\widehat{U}_{\rm o}$ with eigenvalue λ_m gives a normalized eigenmode $|m'\rangle$ of $\widehat{U}'_{\rm o}$ with eigenvalue λ_m according to Eq. (20).

(b) For each eigenstate $|m'\rangle$ of $\widehat{U}'_{\rm o}$ with eigenvalue λ'_m, the state $(\widehat{\mathbf{1}} - \widehat{P}_{\mathcal{L}})|m'\rangle$ is an eigenstate of $\widehat{U}_{\rm o}$ with the same eigenvalue λ'_m,

$$\widehat{U}_{\rm o}(\widehat{\mathbf{1}} - \widehat{P}_{\mathcal{L}})|m'\rangle \overset{(14)}{=} (\widehat{\mathbf{1}} - \widehat{P}_{\mathcal{L}})\widehat{U}(\widehat{\mathbf{1}} - \widehat{P}_{\mathcal{L}})^2|m'\rangle, \tag{B7}$$

$$= (\widehat{\mathbf{1}} - \widehat{P}_{\mathcal{L}})\widehat{U}(\widehat{\mathbf{1}} - \widehat{P}_{\mathcal{L}})|m'\rangle, \tag{B8}$$

$$\overset{(17)}{=} (\widehat{\mathbf{1}} - \widehat{P}_{\mathcal{L}})\widehat{U}'_{\rm o}|m'\rangle, \tag{B9}$$

$$\overset{(B2)}{=} \lambda'_m(\widehat{\mathbf{1}} - \widehat{P}_{\mathcal{L}})|m'\rangle. \tag{B10}$$

This further shows that for nonzero eigenvalue λ'_m the normalized eigenmode $|m'\rangle$ of $\widehat{U}'_{\rm o}$ gives a normalized eigenmode $|m\rangle$ of $\widehat{U}_{\rm o}$ according to Eq. (19).

APPENDIX C: DETAILS OF THE INTEGRABLE APPROXIMATION

In this Appendix we summarize some technical aspects on the integrable approximation. Computational details of the classical integrable approximation as well as slight changes as compared to Ref. [46] are given in Sec. C 1. Details of the quantization are discussed in Sec. C 2 in the Appendix.

1. Details of the classical integrable approximation

We now summarize the modifications of the algorithm described in Ref. [46] in order to account for the symmetries of our system. Then we give a list of relevant computational parameters.

a. Symmetrization

In agreement with Ref. [46], the canonical transformation $\mathcal{T}$, Eq. (23), is composed of (i) an initial canonical transformation,

$$\mathcal{T}^0 : (\theta, I) \mapsto (Q, P), \tag{C1}$$

which provides a rough integrable approximation of the regular phase-space region and (ii) a series of canonical near-identity transformations,

$$\mathcal{T}' \equiv \mathcal{T}^{N_\mathcal{T}} \circ \ldots \circ \mathcal{T}^1 : (Q, P) \mapsto (q, p), \tag{C2}$$

which improve the agreement between the shape of the tori of the mixed system and the integrable approximation.

In contrast to Ref. [46], we use the symmetrized standard map in this paper. In order to account for this symmetry, we specify the canonical transformation, Eq. (C1), as

$$\mathcal{T}^0 : \begin{pmatrix} \theta \\ I \end{pmatrix} \mapsto \begin{pmatrix} Q \\ P \end{pmatrix} = \begin{bmatrix} q^\star + \sqrt{2I/\sigma}\cos(\theta) \\ p^\star - \sqrt{2I\sigma}\sin(\theta) \end{bmatrix}. \tag{C3}$$

Here $(q^\star, p^\star) = (0.5, 0.0)$ are the coordinates of the central fixed point in the standard map. The parameter σ is determined from the stability matrix of the standard map at $(q^\star, p^\star)$,

$$\mathcal{M} = \begin{pmatrix} 1 - \frac{\kappa}{2} & 1 \\ -\kappa\left(1 - \frac{\kappa}{4}\right) & 1 - \frac{\kappa}{2} \end{pmatrix} \tag{C4}$$

as [71]

$$\sigma^2 = \frac{\left|1 + \frac{\kappa}{2}\right| - \left|1 - \frac{\kappa}{2}\right|}{\left|1 + \frac{\kappa}{2}\right| + \left|1 - \frac{\kappa}{2}\right|}. \tag{C5}$$

Furthermore, the symmetry of the systems is imposed on the transformations $\mathcal{T}^1, \ldots, \mathcal{T}^{N_\mathcal{T}}$, Eq. (C2), by specifying their generating function as

$$F^a(q, p') = qp' + \sum_{n=1}^{N_q}\sum_{m=1}^{N_p} a_{m,n} \times \sin(2\pi n[q - q^\star])\sin(2\pi m[p' - p^\star]), \tag{C6}$$

rather than using the more general form of Ref. [46, Eq. (31)].

b. Algorithmic overview

(i) We determine the parameters $I_{r:s}$, $M_{r:s}$, $V_{r:s}$, ϕ_0, Eq. (22), as described in Ref. [31].

(ii) We determine $\mathcal{H}_0(I)$, Eq. (22b), by fitting it to $N_{\text{tori, disp}}$ tuples of action and frequency $(\bar{J}, \bar{\omega})$ describing the tori of the regular region in the corotating frame of the resonance.

(iii) We determine the near-identity transformations of Eq. (C2). Initially, this requires sampling of the regular region using N_{ang} points along N_{tori} tori. The invertibility of the near-identity transformations in a certain phase-space region is ensured by rescaling the coefficients $a_{m,n} \mapsto \eta a_{m,n}$ in Eq. (C6) using a damping factor η. If N_q, N_p in Eq. (C6) are too large, then the tori of the integrable approximation form curls and tendrils in the chaotic region. In that case, the integrable approximation cannot predict decay rates. We control this problem by choosing the largest possible parameters N_q, N_p for which the tori of the integrable approximation provide a smooth extrapolation into the chaotic phase-space region. After a finite amount of steps $N_\mathcal{T}$, the canonical transformations do not improve the agreement between the regular region and the integrable approximation. At this point, we terminate the algorithm.

c. Computational parameters

In the following we list the important parameters of the integrable approximation.

For $\kappa = 2.9$ we use $I_{r:s} = 0.009223$, $M_{r:s} = 0.06243$, $V_{r:s} = -1.655 \times 10^{-7}$, and $\phi_0 = \pi$. For $\mathcal{H}_0$ in Eq. (22b) we

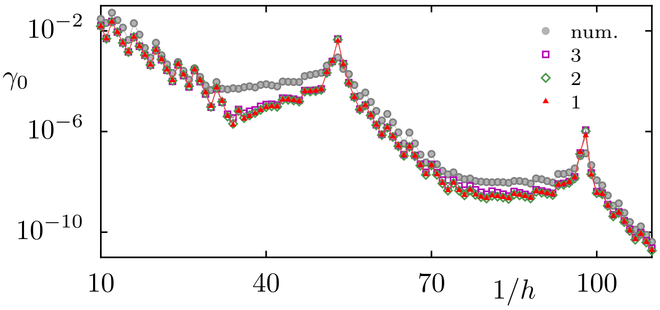

FIG. 11. Decay rates γ_0 for the standard map at $\kappa = 3.4$ versus the inverse effective Planck constant. Numerically determined rates [(gray) circles] are compared to predicted rates according to Eq. (2) [(colored) symbols] based on three slightly different integrable approximations.

used $N_{\text{disp}} = 4$ and fit its derivative to $N_{\text{tori, disp}} = 120$ tori of noble frequency. We use $N_{\mathcal{T}} = 40$ near-identity transformations, Eq. (C2), generated from Eq. (C6) with $N_q = N_p = 2$ and coefficients rescaled by $\eta = 0.05$. The regular region was sampled using $N_{\text{ang}} = 200$ points along $N_{\text{tori}} = 120$ tori, equidistantly distributed in action.

For $\kappa = 3.4$ we use $I_{r:s} = 0.01026$, $M_{r:s} = -0.047$, $V_{r:s} = -1.612 \times 10^{-5}$, and $\phi_0 = 0$. For $\mathcal{H}_0$ in Eq. (22b) we use $N_{\text{disp}} = 6$ and fit its derivative to $N_{\text{tori, disp}} = 120$ tori, equidistantly distributed in action. We use $N_{\mathcal{T}} = 15$ near-identity transformations, Eq. (C2), generated from Eq. (C6) with $N_q = N_p = 2$ and coefficients rescaled by $\eta = 0.25$. The regular region is sampled using $N_{\text{ang}} = 300$ points along $N_{\text{tori}} = 120$ tori, equidistantly distributed in action.

For $\kappa = 3.5$ we use $I_{r:s} = 0.01244$, $M_{r:s} = -0.048$, $V_{r:s} = -2.98 \times 10^{-5}$, and $\phi_0 = 0$. For $\mathcal{H}_0$ in Eq. (22b) we use $N_{\text{disp}} = 4$ and fit its derivate to $N_{\text{tori, disp}} = 120$ tori, equidistantly distributed in action. We use $N_{\mathcal{T}} = 15$ near-identity transformations, Eq. (C2), generated from Eq. (C6) with $N_q = N_p = 2$ and coefficients rescaled by $\eta = 0.25$. The regular region is sampled using $N_{\text{ang}} = 300$ points along $N_{\text{tori}} = 120$ tori, equidistantly distributed in action.

d. Robustness

After fixing all parameters as described above, the final integrable approximation might differ, depending on the sampling of the regular region. In order to show that this does not affect the final prediction, we evaluate Eq. (2) for three integrable approximations which are based on slightly different sets of sample points. The result is illustrated in Fig. 11. It shows that the prediction is clearly robust.

2. Derivation of quantization

In the following, we sketch the basic ideas leading to the quantization procedure presented in Sec. IV C. To this end we first present the quantization of the Hamilton function obtained after the transformation $\mathcal{T}^0$, Eqs. (C1) and (C3), in Sec. C 2 a. In Sec. C 2 b we present how we extend these results to the full transformation $\mathcal{T}$.

a. Quantization after $\mathcal{T}^0$

To quantize the Hamilton function $H^{(0)}_{r:s}(Q,P)$ obtained after the canonical transformation $\mathcal{T}^0$, Eqs. (C1) and (C3), we follow Ref. [43] by starting with the transformed Hamilton-function

$$H^{(0)}_{r:s}(Q,P) = \mathcal{H}_0\left(\frac{Q^2+P^2}{2}\right) + \frac{V_{r:s}}{(2I_{r:s})^{r/2}} \times \left[\exp(i\phi_0)\left(\sigma^{1/2}[Q-q^\star] - i\frac{P}{\sigma^{1/2}}\right)^r + \exp(-i\phi_0)\left(\sigma^{1/2}[Q-q^\star] + i\frac{P}{\sigma^{1/2}}\right)^r\right]. \tag{C7}$$

In order to quantize this function, we replace the coordinates (Q,P) by operators

$$Q \mapsto \widehat{Q}, \tag{C8a}$$

$$P \mapsto \widehat{P}, \tag{C8b}$$

and demand the usual commutation relation

$$[\widehat{Q},\widehat{P}] = i\hbar. \tag{C9}$$

This allows for introducing the corresponding ladder operators as

$$\widehat{a} := \frac{1}{(2\hbar)^{1/2}}\left(\sigma^{1/2}[\widehat{Q} - q^\star] + i\frac{\widehat{P}}{\sigma^{1/2}}\right), \tag{C10a}$$

$$\widehat{a}^\dagger := \frac{1}{(2\hbar)^{1/2}}\left(\sigma^{1/2}[\widehat{Q} - q^\star] - i\frac{\widehat{P}}{\sigma^{1/2}}\right), \tag{C10b}$$

which admit the commutator

$$[\widehat{a},\widehat{a}^\dagger] = 1, \tag{C11}$$

such that we get the number operator

$$\widehat{n} := \widehat{a}^\dagger\widehat{a}. \tag{C12}$$

Based on these operators, the quantization of $H^{(0)}_{r:s}$ takes the form [43]

$$\widehat{H}^{(0)}_{r:s} = \mathcal{H}_0(\widehat{I}) + V_{r:s}\left(\frac{\hbar}{I_{r:s}}\right)^{\frac{r}{2}}[\widehat{a}^{\dagger r}\exp(i\phi_0) + \widehat{a}^r\exp(-i\phi_0)], \tag{C13}$$

where

$$\widehat{I} := \hbar(\widehat{n} + 1/2) \tag{C14}$$

is the operator replacing the unperturbed action I. Finally, in order to define the basis states, we identify them with the eigenstates of the number operator leading to

$$\widehat{I}\big|I_n^{(0)}\big\rangle = I_n\big|I_n^{(0)}\big\rangle, \tag{C15}$$

where the eigenvalues become quantizing actions $I_n = \hbar(n + 1/2)$ and the basis states $|I_n^{(0)}\rangle$ fulfill

$$\widehat{a}\big|I_0^{(0)}\big\rangle = 0, \tag{C16a}$$

$$\big|I_n^{(0)}\big\rangle = \frac{1}{\sqrt{n!}}\widehat{a}^{\dagger^n}\big|I_0^{(0)}\big\rangle. \tag{C16b}$$

With respect to this position basis $|I_n^{(0)}\rangle$ become the eigenstates of the harmonic oscillator

$$\big\langle Q\big|I_n^{(0)}\big\rangle = \left(\frac{\sigma}{\pi\hbar}\right)^{\frac{1}{4}}\frac{1}{\sqrt{2^n n!}}\,\mathrm{H}_n\!\left(\frac{Q}{\sqrt{\hbar/\sigma}}\right)\exp\!\left(-\frac{\sigma Q^2}{2\hbar}\right), \tag{C17}$$

where $\mathrm{H}_n(\cdot)$ are the Hermite polynomials.

b. Quantization after $\mathcal{T}$

Our final goal is of course to obtain the quantization of the Hamilton function $H_{r:s}(q,p)$, which is related to $H_{r:s}^{(0)}(Q,P)$ via the canonical transformation $\mathcal{T}'$, Eq. (C2). In order to obtain its quantization, we assume that $\mathcal{T}'$ quantum-mechanically corresponds to a unitary operator $\widehat{U}_{\mathcal{T}'}$ which has the following properties:

$$\widehat{U}_{\mathcal{T}'}^{-1} = \widehat{U}_{\mathcal{T}'^{-1}}, \tag{C18a}$$

$$\widehat{Q}' = \widehat{U}_{\mathcal{T}'}\widehat{Q}\widehat{U}_{\mathcal{T}'}^{-1}, \tag{C18b}$$

$$\widehat{P}' = \widehat{U}_{\mathcal{T}'}\widehat{P}\widehat{U}_{\mathcal{T}'}^{-1}. \tag{C18c}$$

Such an operator exists at least within a semiclassical approximation [74]. Note that $\widehat{Q}',\widehat{P}'$ represent the operators $\widehat{Q},\widehat{P}$ within the final coordinate frame (q,p). However, they must not be confused with the operators $\widehat{q},\widehat{p}$ which give rise to the position and momentum basis in the final coordinate frame (q,p). In particular, while $\widehat{q}|q\rangle = q|q\rangle$, $\widehat{Q}|q\rangle \neq q|q\rangle$.

Under the above assumption the transformed operators preserve the commutation relation

$$[\widehat{Q}',\widehat{P}'] = i\hbar. \tag{C19}$$

Furthermore, we get the transformed ladder operators as

$$\widehat{a}' := \widehat{U}_{\mathcal{T}'}\widehat{a}\widehat{U}_{\mathcal{T}'}^{-1}, \tag{C20a}$$

$$\widehat{a}'^{\dagger} := \widehat{U}_{\mathcal{T}'}\widehat{a}^{\dagger}\widehat{U}_{\mathcal{T}'}^{-1}, \tag{C20b}$$

which admit the same commutator

$$[\widehat{a}',\widehat{a}'^{\dagger}] = 1, \tag{C21}$$

such that we get the transformed number operator

$$\widehat{n}' = \widehat{U}_{\mathcal{T}'}\widehat{n}\widehat{U}_{\mathcal{T}'}^{-1}, \tag{C22}$$

and the transformed action operator

$$\widehat{I}' := \hbar(\widehat{n}' + 1/2). \tag{C23}$$

Based on these operators, we can define the transformation of the quantization of $H_{r:s}^{(0)}(Q,P)$ which we identify with the quantization of $H_{r:s}(q,p)$. It takes the form [43]

$$\widehat{H}_{r:s} = \mathcal{H}_0(\widehat{I}') + V_{r:s}\left(\frac{\hbar}{I_{r:s}}\right)^{\frac{r}{2}}[\widehat{a}'^{\dagger^r}\exp(i\phi_0) + \widehat{a}'^{r}\exp(-i\phi_0)]. \tag{C24}$$

Finally, in order to define the basis states $|I_n\rangle$, we identify them with the eigenstates of the number operator $\widehat{n}'$, such that

$$\widehat{I}'|I_n\rangle = I_n|I_n\rangle \tag{C25}$$

with the basis states $|I_n\rangle$ which admit the property

$$\widehat{a}'|I_0\rangle = 0, \tag{C26a}$$

$$|I_n\rangle = \frac{1}{\sqrt{n!}}\widehat{a}'^{\dagger^n}|I_0\rangle. \tag{C26b}$$

Evaluating $\widehat{H}_{r:s}$, Eq. (C24), in the basis of $|I_n\rangle$, based on Eqs. (C26) gives the matrix representation of Eq. (26).

Finally, for connecting $\widehat{H}_{r:s}$ and $\widehat{U}$ we require the basis states with respect to the basis $|q\rangle$. To this end, one can show from the above equations that

$$|I_n\rangle = \widehat{U}_{\mathcal{T}'}\big|I_n^{(0)}\big\rangle, \tag{C27}$$

such that

$$\langle q|I_n\rangle = \int dQ\langle q|\widehat{U}_{\mathcal{T}'}|Q\rangle\big\langle Q\big|I_n^{(0)}\big\rangle. \tag{C28}$$

In principle, the operator $\langle q|\widehat{U}_{\mathcal{T}'}|Q\rangle$ can be evaluated semiclassically, using the techniques described in Ref. [74]. However, this does not give an analytical closed form result and its evaluation is numerically extremely tedious. Furthermore, $\widehat{U}_{\mathcal{T}'}$ is usually so close to an identity transformation such that a semiclassical evaluation of $\langle q|\widehat{U}_{\mathcal{T}'}|Q\rangle$ contains too many turning points.

Hence, we take an alternative approach, which is numerically feasible: (i) We recognize that the states $|I_n\rangle$ are the eigenstates of the operator $\widehat{I}$, originating from the phase-space coordinate I. (ii) We define the function $I(q,p)$ which is obtained after the full canonical transformation $\mathcal{T}$. (iii) We define the Weyl quantization of this function on a phase-space torus giving the Hermitian matrix of Eq. (25). (iv) We diagonalize this matrix numerically, yielding the states $\langle\bar{q}_l|I_n\rangle$.

Finally, obtaining the modes $\langle\bar{q}_l|I_n\rangle$ from an eigenvalue equation comes at the cost that their relative phase [usually ensured via Eq. (C26) or, alternatively, via Eqs. (C16) and (C27)] is lost. For the standard map we try to restore this phase by exploiting the symmetry of Eq. (25), which for our system becomes a real symmetric matrix, in that we can ensure that the coefficient vector $\langle\bar{q}_l|I_n\rangle$ can be chosen real. Finally, we fix the sign of this coefficient vector by aligning it with the mode $\langle Q|I_n^{(0)}\rangle$ defined via Eq. (C17). This means that we choose the sign of the coefficient vector $\langle\bar{q}_l|I_n\rangle$ such that the following relation is fulfilled:

$$\sum_n \langle I_n|\bar{q}_l\rangle\big[\big\langle Q\big|I_n^{(0)}\big\rangle\big]\big|_{Q=\bar{q}_l} > 0. \tag{C29}$$

This assumes that the unitary operator representing the quantum canonical transformation in Eq. (C28) is sufficiently close to an identity transformation $\widehat{U}_{\mathcal{T}'} \approx 1$.

[1] M. J. Davis and E. J. Heller, Quantum dynamical tunneling in bound states, J. Chem. Phys. **75**, 246 (1981).

[2] S. Keshavamurthy and P. Schlagheck, *Dynamical Tunneling: Theory and Experiment* (Taylor & Francis, Boca Raton, FL, 2011).

[3] W. A. Lin and L. E. Ballentine, Quantum Tunneling and Chaos in a Driven Anharmonic Oscillator, Phys. Rev. Lett. **65**, 2927 (1990).

[4] O. Bohigas, S. Tomsovic, and D. Ullmo, Manifestations of classical phase space structures in quantum mechanics, Phys. Rep. **223**, 43 (1993).

[5] S. Shinohara, T. Harayama, T. Fukushima, M. Hentschel, T. Sasaki, and E. E. Narimanov, Chaos-Assisted Directional Light Emission from Microcavity Lasers, Phys. Rev. Lett. **104**, 163902 (2010).

[6] S. Shinohara, T. Harayama, T. Fukushima, M. Hentschel, S. Sunada, and E. E. Narimanov, Chaos-assisted emission from asymmetric resonant cavity microlasers, Phys. Rev. A **83**, 053837 (2011).

[7] J. Yang, S.-B. Lee, S. Moon, S.-Y. Lee, S. W. Kim, T. T. A. Dao, J.-H. Lee, and K. An, Pump-Induced Dynamical Tunneling in a Deformed Microcavity Laser, Phys. Rev. Lett. **104**, 243601 (2010).

[8] H. Kwak, Y. Shin, S. Moon, S.-B. Lee, J. Yang, and K. An, Nonlinear resonance-assisted tunneling induced by microcavity deformation, Sci. Rep. **5**, 9010 (2015).

[9] C.-H. Yi, H.-H. Yu, J.-W. Lee, and C.-M. Kim, Fermi resonance in optical microcavities, Phys. Rev. E **91**, 042903 (2015).

[10] C.-H. Yi, H.-H. Yu, and C.-M. Kim, Resonant torus-assisted tunneling, Phys. Rev. E **93**, 012201 (2016).

[11] C. Dembowski, H.-D. Gräf, A. Heine, R. Hofferbert, H. Rehfeld, and A. Richter, First Experimental Evidence for Chaos-Assisted Tunneling in a Microwave Annular Billiard, Phys. Rev. Lett. **84**, 867 (2000).

[12] A. Bäcker, R. Ketzmerick, S. Löck, M. Robnik, G. Vidmar, R. Höhmann, U. Kuhl, and H.-J. Stöckmann, Dynamical Tunneling in Mushroom Billiards, Phys. Rev. Lett. **100**, 174103 (2008).

[13] B. Dietz, T. Guhr, B. Gutkin, M. Miski-Oglu, and A. Richter, Spectral properties and dynamical tunneling in constant-width billiards, Phys. Rev. E **90**, 022903 (2014).

[14] S. Gehler, S. Löck, S. Shinohara, A. Bäcker, R. Ketzmerick, U. Kuhl, and H.-J. Stöckmann, Experimental Observation of Resonance-Assisted Tunneling, Phys. Rev. Lett. **115**, 104101 (2015).

[15] W. K. Hensinger *et al.*, Dynamical tunneling of ultracold atoms, Nature **412**, 52 (2001).

[16] D. A. Steck, W. H. Oskay, and M. G. Raizen, Observation of chaos-assisted tunneling between islands of stability, Science **293**, 274 (2001).

[17] T. Uzer, D. W. Noid, and R. A. Marcus, Uniform semiclassical theory of avoided crossings, J. Chem. Phys. **79**, 4412 (1983).

[18] A. M. Ozorio de Almeida, Tunneling and the semiclassical spectrum for an isolated classical resonance, J. Phys. Chem. **88**, 6139 (1984).

[19] O. Brodier, P. Schlagheck, and D. Ullmo, Resonance-Assisted Tunneling in Near-Integrable Systems, Phys. Rev. Lett. **87**, 064101 (2001).

[20] O. Brodier, P. Schlagheck, and D. Ullmo, Resonance-assisted tunneling, Ann. Phys. (NY) **300**, 88 (2002).

[21] J. Zakrzewski, D. Delande, and A. Buchleitner, Ionization via chaos assisted tunneling, Phys. Rev. E **57**, 1458 (1998).

[22] A. Buchleitner, D. Delande, and J. Zakrzewski, Non-dispersive wave packets in periodically driven quantum systems, Phys. Rep. **368**, 409 (2002).

[23] S. Keshavamurthy, Dynamical tunneling in molecules: Role of the classical resonances and chaos, J. Chem. Phys. **119**, 161 (2003).

[24] S. Keshavamurthy, On dynamical tunneling and classical resonances, J. Chem. Phys. **122**, 114109 (2005).

[25] S. Wimberger, P. Schlagheck, C. Eltschka, and A. Buchleitner, Resonance-Assisted Decay of Nondispersive Wave Packets, Phys. Rev. Lett. **97**, 043001 (2006).

[26] S. Keshavamurthy, Dynamical tunneling in molecules: Quantum routes to energy flow, Int. Rev. Phys. Chem. **26**, 521 (2007).

[27] A. Shudo and K. S. Ikeda, Complex Classical Trajectories and Chaotic Tunneling, Phys. Rev. Lett. **74**, 682 (1995).

[28] A. Shudo and K. S. Ikeda, Chaotic tunneling: A remarkable manifestation of complex classical dynamics in non-integrable quantum phenomena, Physica D **115**, 234 (1998).

[29] V. A. Podolskiy and E. E. Narimanov, Semiclassical Description of Chaos-Assisted Tunneling, Phys. Rev. Lett. **91**, 263601 (2003).

[30] V. A. Podolskiy and E. E. Narimanov, Chaos-assisted tunneling in dielectric microcavities, Opt. Lett. **30**, 474 (2005).

[31] C. Eltschka and P. Schlagheck, Resonance- and Chaos-Assisted Tunneling in Mixed Regular-Chaotic Systems, Phys. Rev. Lett. **94**, 014101 (2005).

[32] M. Sheinman, S. Fishman, I. Guarneri, and L. Rebuzzini, Decay of quantum accelerator modes, Phys. Rev. A **73**, 052110 (2006).

[33] A. Bäcker, R. Ketzmerick, S. Löck, and L. Schilling, Regular-to-Chaotic Tunneling Rates Using a Fictitious Integrable System, Phys. Rev. Lett. **100**, 104101 (2008).

[34] A. Shudo, Y. Ishii, and K. S. Ikeda, Chaos attracts tunneling trajectories: A universal mechanism of chaotic tunneling, Europhys. Lett. **81**, 50003 (2008).

[35] A. Shudo, Y. Ishii, and K. S. Ikeda, Julia sets and chaotic tunneling: I, J. Phys. A **42**, 265101 (2009).

[36] A. Shudo, Y. Ishii, and K. S. Ikeda, Julia sets and chaotic tunneling: II, J. Phys. A **42**, 265102 (2009).

[37] A. Bäcker, R. Ketzmerick, S. Löck, J. Wiersig, and M. Hentschel, Quality factors and dynamical tunneling in annular microcavities, Phys. Rev. A **79**, 063804 (2009).

[38] A. Bäcker, R. Ketzmerick, and S. Löck, Direct regular-to-chaotic tunneling rates using the fictitious-integrable-system approach, Phys. Rev. E **82**, 056208 (2010).

[39] S. Löck, A. Bäcker, R. Ketzmerick, and P. Schlagheck, Regular-to-Chaotic Tunneling Rates: From the Quantum to the Semiclassical Regime, Phys. Rev. Lett. **104**, 114101 (2010).

[40] N. Mertig, S. Löck, A. Bäcker, R. Ketzmerick, and A. Shudo, Complex paths for regular-to-chaotic tunneling rates, Europhys. Lett. **102**, 10005 (2013).

[41] Y. Hanada, A. Shudo, and K. S. Ikeda, Origin of the enhancement of tunneling probability in the nearly integrable system, Phys. Rev. E **91**, 042913 (2015).

[42] J. Kullig and J. Wiersig, Q spoiling in deformed optical microdisks due to resonance-assisted tunneling, Phys. Rev. E **94**, 022202 (2016).

[43] P. Schlagheck, A. Mouchet, and D. Ullmo, Resonance-assisted tunneling in mixed regular-chaotic systems, in *Dynamical Tunneling: Theory and Experiment*, [2], Chap. 8, p. 177.

[44] J. Le Deunff and A. Mouchet, Instantons re-examined: Dynamical tunneling and resonant tunneling, Phys. Rev. E **81**, 046205 (2010).

[45] J. Le Deunff, A. Mouchet, and P. Schlagheck, Semiclassical description of resonance-assisted tunneling in one-dimensional integrable models, Phys. Rev. E **88**, 042927 (2013).

[46] J. Kullig, C. Löbner, N. Mertig, A. Bäcker, and R. Ketzmerick, Integrable approximation of regular regions with a nonlinear resonance chain, Phys. Rev. E **90**, 052906 (2014).

[47] F. Fritzsch, A. Bäcker, R. Ketzmerick, and N. Mertig, Complex-path prediction of resonance-assisted tunneling in mixed systems, arXiv:1609.09276 [nlin.CD].

[48] B. V. Chirikov, A universal instability of many-dimensional oscillator systems, Phys. Rep. **52**, 263 (1979).

[49] A. N. Kolmogorov, Preservation of conditionally periodic movements with small change in the Hamilton function (in Russian), Dokl. Akad. Nauk. SSSR **98**, 527 (1954), english translation in [75], 51–56.

[50] V. I. Arnold, Small denominators and problems of stability of motion in classical and celestial mechanics, Russ. Math. Surv. **18**, 85 (1963).

[51] V. I. Arnold, Proof of a theorem of A. N. Kolmogorov on the invariance of quasi-periodic motions under small perturbations of the Hamiltonian, Russ. Math. Surv. **18**, 9 (1963).

[52] J. Moser, On invariant curves of area-preserving mappings of an annulus, Nachr. Akad. Wiss. Göttingen **1**, 1 (1962).

[53] G. D. Birkhoff, Proof of Poincaré's geometric theorem, Trans. Am. Math. Soc. **14**, 14 (1913).

[54] A. J. Lichtenberg and M. A. Lieberman, *Regular and Chaotic Motion*, Vol. 38 of Applied Mathematical Sciences, 2nd ed. (Springer-Verlag, New York (1992).

[55] M. V. Berry, N. L. Balazs, M. Tabor, and A. Voros, Quantum maps, Ann. Phys. (NY) **122**, 26 (1979).

[56] J. H. Hannay and M. V. Berry, Quantization of linear maps on a torus—Fresnel diffraction by a periodic grating, Physica D **1**, 267 (1980).

[57] S.-J. Chang and K.-J. Shi, Evolution and exact eigenstates of a resonant quantum system, Phys. Rev. A **34**, 7 (1986).

[58] J. P. Keating, F. Mezzadri, and J. M. Robbins, Quantum boundary conditions for torus maps, Nonlinearity **12**, 579 (1999).

[59] M. Degli Esposti and S. Graffi, Mathematical aspects of quantum maps, in *The Mathematical Aspects of Quantum Maps*, [76], p. 49.

[60] A. Bäcker, Numerical aspects of eigenvalues and eigenfunctions of chaotic quantum systems, in *Degli Esposti and Graffi* [76], p. 91.

[61] I. C. Percival, Regular and irregular spectra, J. Phys. B **6**, L229 (1973).

[62] M. V. Berry, Regular and irregular semiclassical wavefunctions, J. Phys. A **10**, 2083 (1977).

[63] A. Voros, Semi-classical ergodicity of quantum eigenstates in the Wigner representation, in Casati and Ford [75], 326.

[64] N. Bohr, On the constitution of atoms and molecules, Philosophical Magazine Series 6 **26**, 1 (1913).

[65] N. Bohr, On the constitution of atoms and molecules. Part II.–Systems containing only a single nucleus, Philos. Mag. Ser. 6 **26**, 476 (1913).

[66] A. Sommerfeld, Zur Quantentheorie der Spektrallinien, Ann. Phys. **356**, 1 (1916).

[67] D. A. Wisniacki, M. Saraceno, F. J. Arranz, R. M. Benito, and F. Borondo, Poincaré-Birkhoff theorem in quantum mechanics, Phys. Rev. E **84**, 026206 (2011).

[68] D. A. Wisniacki, Universal wave functions structure in mixed systems, Europhys. Lett. **106**, 60006 (2014).

[69] D. A. Wisniacki and P. Schlagheck, Quantum manifestations of classical nonlinear resonances, Phys. Rev. E **92**, 062923 (2015).

[70] J. D. Hanson, E. Ott, and T. M. Antonsen, Influence of finite wavelength on the quantum kicked rotator in the semiclassical regime, Phys. Rev. A **29**, 819 (1984).

[71] C. Löbner, S. Löck, A. Bäcker, and R. Ketzmerick, Integrable approximation of regular islands: The iterative canonical transformation method, Phys. Rev. E **88**, 062901 (2013).

[72] R. S. MacKay, J. D. Meiss, and I. C. Percival, Stochasticity and Transport in Hamiltonian Systems, Phys. Rev. Lett. **52**, 697 (1984).

[73] R. S. MacKay, J. D. Meiss, and I. C. Percival, Transport in Hamiltonian systems, Physica D **13**, 55 (1984).

[74] E. B. Bogomolny, Semiclassical quantization of multidimensional systems, Nonlinearity **5**, 805 (1992).

[75] G. Casati and J. Ford (eds.), *Stochastic Behavior in Classical and Quantum Hamiltonian Systems*, Vol. 93 of Lecture Notes in Physics (Springer-Verlag, Berlin, 1979).

[76] M. Degli Esposti and S. Graffi (eds.), *The Mathematical Aspects of Quantum Maps*, Vol. 618 of Lecture Notes in Physics (Springer-Verlag, Berlin, 2003).